MATERIALS CHEMISTRY FRONTIERS

REVIEW

View Article Online
View Journal | View Issue

Cite this: *Mater. Chem. Front.*, 2020, **4**, 2256

Functionalization of fullerene materials toward applications in perovskite solar cells†

Lingbo Jia, Muqing Chen * and Shangfeng Yang *

Fullerene materials exhibit high electron affinity, high electron mobility and small reorganization energy, thus they have been widely utilized as electron transport layers, cathode interfacial layers and trap passivators in constructing efficient organic–inorganic hybrid halide perovskite solar cells (PSCs). Herein, we summarize the recent progress of functionalized fullerene materials (*i.e.*, fullerene derivatives) which have been applied in PSCs, focusing on chemical functionalization strategies. We provide exhaustive lists of all reported fullerene derivatives applied in PSCs, and categorize them based on the types of addend groups and addition patterns. In particular, we manage to unveil the correlation between the chemical structures of fullerene derivatives, especially the addend groups, and their performance in improving the PSC device efficiency and stability. Finally, we propose an outlook on the future development of fullerene derivatives in realizing high-performance PSC devices.

Received 7th May 2020,
Accepted 10th June 2020

DOI: 10.1039/d0qm00295j

rsc.li/frontiers-materials

1. Introduction

Organic–inorganic hybrid halide perovskites with a general formula of ABX_3 (Fig. 1a), where A^+ is $CH_3NH_3^+$, $NH_2CH{=}NH_2^+$, Cs^+, Rb^+ *etc.*, B^{2+} is Pb^{2+} or Sn^{2+} and X^- is I^-, Br^- or Cl^-, are emerging optoelectronic materials with the advantages of tunable optical bandgaps, high absorption coefficients, long charge carrier diffusion lengths, small exciton binding energies, and high carrier mobilities; thus they have been receiving considerable attention in the widespread fields of photovoltaics, light-emitting diodes, sensors and photodetectors *etc.*[1–7] In particular, since the first demonstration of applying $CH_3NH_3PbX_3$ (X = Br, I) in dye-sensitized solar cells as sensitizers in 2009,[8] perovskite solar cells (PSCs) using the organic–inorganic hybrid halide perovskites as light-absorbing layers

Hefei National Laboratory for Physical Sciences at Microscale, CAS Key Laboratory of Materials for Energy Conversion, Anhui Laboratory of Advanced Photon Science and Technology & Department of Materials Science and Engineering, University of Science and Technology of China, Hefei 230026, China.
E-mail: mqchen@ustc.edu.cn, sfyang@ustc.edu.cn

† Electronic supplementary information (ESI) available. See DOI: 10.1039/d0qm00295j

Lingbo Jia

Lingbo Jia is currently a PhD candidate in Prof. Shangfeng Yang's group in the University of Science and Technology of China. Her research interests focus on the synthesis of novel fullerene derivatives and their applications in perovskite solar cells.

Muqing Chen

Muqing Chen obtained his PhD degree in materials science of the University of Science and Technology of China in 2012. He later became a postdoctoral in the college of materials science and engineering of the university of Science and Technology of Huazhong. In October 2017, he joined the group of Professor Shangfeng Yang as an Associate Professor in the Department of Materials Science and Engineering of the University of Science and Technology of China. His research interests are to explore the chemical properties and applications of fullerene including endohedral metallofullerenes in the fields of materials science, catalysis, energy storage and conversion.

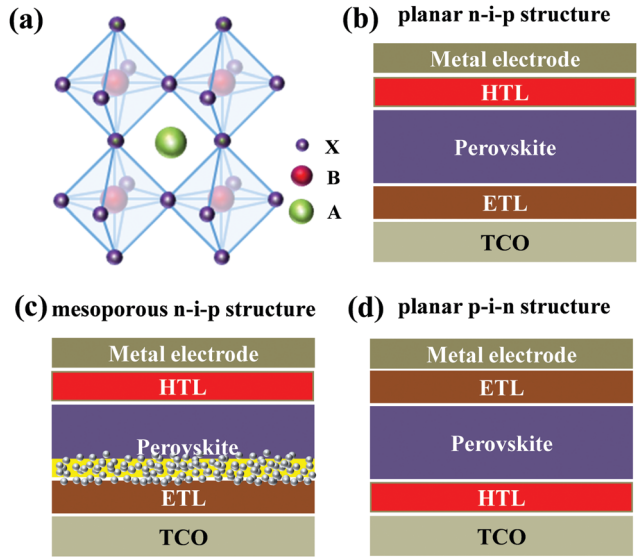

Fig. 1 (a) Crystal structure of ABX_3 perovskite light-absorbing materials. The common device architectures of (b) planar n–i–p structures, (c) mesoporous n–i–p structures, and (d) planar p–i–n structures. TCO refers to transparent conductive oxide.

have been rapidly developed during the past decade, and the record certified power conversion efficiency (PCE) has reached 25.2%.[9] Such a high PCE becomes competitive with the commercialized crystalline-Si and inorganic semiconductor thin film solar cells, rendering bright prospects of PSCs toward efficient utilization of sustainable energy.[10]

For the state-of-the-art PSC devices, their architectures can be generally categorized into three main types: mesoporous n–i–p structures, planar n–i–p structures and planar p–i–n structures (Fig. 1b–d), where n refers to an n-type semiconductor functioning as an electron transporting layer (ETL), i represents a perovskite, and p denotes a p-type semiconductor acting as a hole transporting layer (HTL).[11–15] Although tremendous advances have been accomplished for PSCs during the past decade, further improvements of both device efficiency and stability are still urgently desired so as to meet the requirement of large-scale commercial applications. Besides, up to now high-efficiency PSC devices are mostly achieved for lead (Pb)-based perovskites, and the environmental toxicity of Pb raises another challenge of PSC application.[16]

To improve the PSC device efficiency and stability, modulating the composition, phase and morphology of perovskite light-absorbing layers and engineering the perovskite/electrode interfaces has been implemented in addition to optimizing the device structure.[17–25] For these strategies, since fullerene materials exhibit high electron affinity, high electron mobility and small reorganization energy, fullerenes have been widely utilized in PSCs by means of being incorporated as interfacial materials between perovskite layers and electrodes or as additives within perovskite layers. In this way, fullerenes behave as electron transport layers, cathode interfacial layers or trap passivators.[6,14,26] Interestingly, versatile roles of fullerenes in PSCs have been identified, revealing that fullerenes can not only facilitate electron extraction and transport due to the strong electron-accepting ability upon being incorporated as interfacial modification layers, but can also lead to defect passivation on the perovskite surface and grain boundaries when introduced as additives within perovskite layers.[27–29]

In this review, we present a comprehensive summary on recent advances in applications of functionalized fullerene materials (*i.e.*, fullerene derivatives) in PSCs. Although there have been several review papers related to applications of fullerenes in PSCs as well, these papers either cover broad topics such as both organic and perovskite solar cells or emphasize merely single aspects,[6,14,26,30–32] while a dedicated review focused on chemical functionalization strategies of fullerene derivatives and the correlations between their chemical structures, especially the addend groups, and functions in PSCs is desirably needed. Herein, we emphasize the synthetic strategies of fullerene derivatives and the importance of their addend groups in improving the performance of PSCs. Based on exhaustive lists of all reported fullerene derivatives applied in PSCs, we categorize them into five groups according to the types of addend groups and addition patterns. In particular, we manage to unveil the correlation between the chemical structures of fullerene derivatives, especially the addend groups, and their performance in improving the PSC device efficiency and stability. Finally, we propose our perspective on the future development of fullerene derivatives in realizing high-performance PSC devices.

2. $PC_{61}BM$ and $PC_{61}BM$-based fullerene derivatives

[6,6]-Phenyl C_{61}-butyric acid methyl ester ($PC_{61}BM$, Fig. 2) is the most widely used ETL of p–i–n (*i.e.*, inverted-structure) PSCs, and was first applied by Chen and co-workers in 2013. $PC_{61}BM$ possesses a suitable lowest unoccupied molecular orbital (LUMO) energy level, which matches with the valence band

Shangfeng Yang

Shangfeng Yang received his PhD from the Hong Kong University of Science and Technology in 2003. He then joined the Leibniz Institute for Solid State and Materials Research (IFW) Dresden, Germany as a Humboldt Fellow. In Dec. 2007 he joined the University of Science and Technology of China as a full time professor of the Hefei National Laboratory for Physical Sciences at Microscale & Department of Materials Science and Engineering. His research interests include the synthesis of fullerene-based nanocarbons and applications in energy conversion and storage. He was the recipient of the National Science Fund for Distinguished Young Scholars and elected a Fellow of the RSC (FRSC).

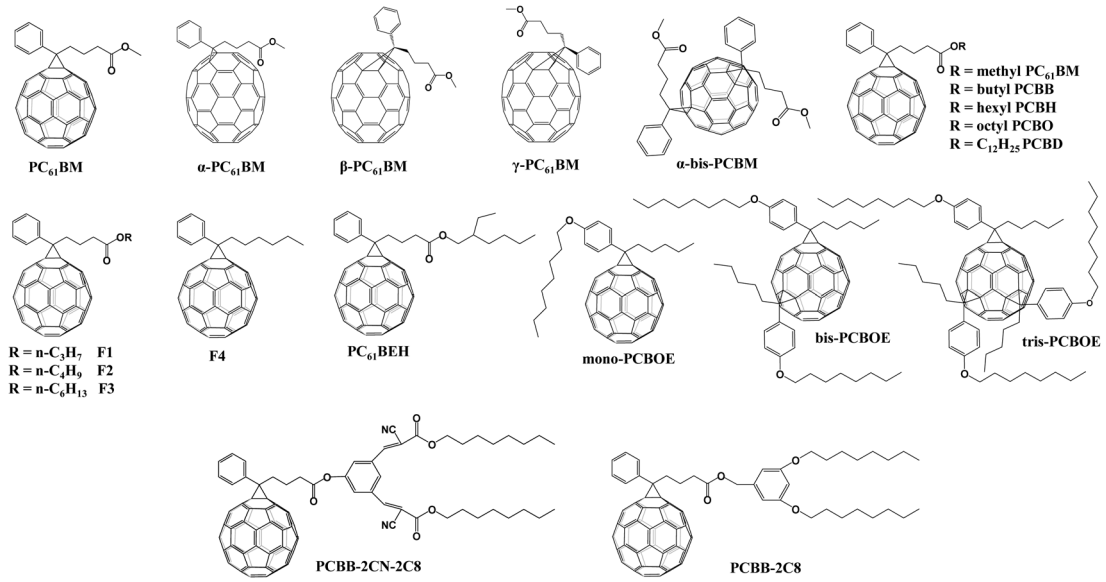

Fig. 2 Molecular structures of $PC_{61}BM$ and $PC_{61}BM$-based fullerene derivatives applied in PSCs.

energy level of $CH_3NH_3PbI_3$ perovskite, leading to enhanced electron transport from the perovskite layer to the $PC_{61}BM$ ETL. As a result, a PCE of 3.9% was achieved for p–i–n $CH_3NH_3PbI_3$ PSC devices.[33] In 2014, Huang and co-workers found that $PC_{61}BM$ deposited on top of the $CH_3NH_3PbI_3$ layer can reduce the trap-states of perovskite films by two orders of magnitude (Fig. 3a), resulting in a moderate PCE of 14.9% for PSC devices along with suppressed photocurrent hysteresis.[34] Later on, the same group reported that reducing the disorder of the $PC_{61}BM$ layer by a simple solvent annealing method (Fig. 3b) is beneficial to increase the open-circuit voltage (V_{oc}) of $CH_3NH_3PbI_3$ PSC devices without sacrificing either short-circuit current (J_{sc}) or the fill factor (FF). This study further pointed out that the ordered $PC_{61}BM$ assembly leads to a significant decrease in the electronic density of states along with an increase in the quasi-Fermi level of the photogenerated electrons (E_{Fn}), contributing

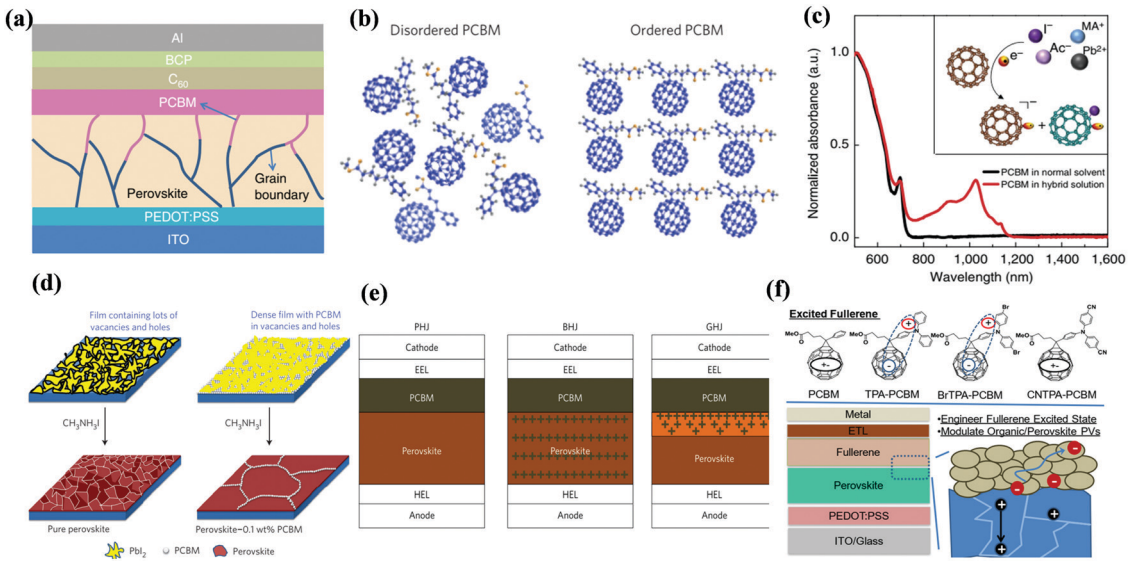

Fig. 3 (a) Device structure of p–i–n perovskite solar cells with a $PC_{61}BM$ layer. Reproduced with permission from ref. 34. Copyright 2014, Nature Publishing Group. (b) Schematic of disordered and ordered $PC_{61}BM$ structures and energy disorder of the $PC_{61}BM$ layer influences the device V_{oc}. Reproduced with permission from ref. 35. Copyright 2016, Nature Publishing Group. (c) Halide-induced deep trap *in situ* passivation and ultraviolet-visible absorption spectroscopy of the interaction between $PC_{61}BM$ and the perovskite in different solutions. Reproduced with permission from ref. 28. Copyright 2015, Nature Publishing Group. (d) Formation of perovskite grains with and without $PC_{61}BM$. Reproduced with permission from ref. 42. Copyright 2016, Nature Publishing Group. (e) Three types of inverted PSCs with a mixed and graded interlayer. Reproduced with permission from ref. 44. Copyright 2016, Nature Publishing Group. (f) Chemical structures of fullerene derivatives and the CT characters of them deposited atop perovskite films. Reproduced with permission from ref. 51. Copyright 2015, Royal Society of Chemistry.

to the improvements of both V_{oc} and PCE (19.4%).[35] Thereafter, $PC_{61}BM$ became the most commonly used ETL of p–i–n PSCs.[36–38]

[6,6]-Phenyl C_{71}-butyric acid methyl ester ($PC_{71}BM$) as the cousin of $PC_{61}BM$ (Fig. 2) was also applied as an effective ETL in inverted-structure $CH_3NH_3PbI_3$ PSCs in 2014, leading to an improved PCE of 16.31% that resulted from the remarkably higher V_{oc} of 1.05 V and FF of 0.78 relative to that based on $PC_{61}BM$ ETL (9.92%).[39] Later on, Xie and co-workers developed a formulation engineering method to study the effect of different component distribution ratios of $PC_{71}BM$ isomers (α-, β_1- and β_2-$PC_{71}BM$, Fig. 2) on the performance of p–i–n $CH_3NH_3PbI_3$ PSCs. The $PC_{71}BM$ ETL with the optimized ratio of three isomers of $PC_{71}BM$ ($\alpha:\beta_1:\beta_2$ = 17 : 1 : 2) exhibits the highest PCE of 17.56%, which outperformed those of the devices with isomerically pure $PC_{71}BM$ ETLs and other adducts of uncontrolled isomeric ratios due to the reduced molecular aggregation and improved electron transfer.[40]

In addition to acting as an ETL, $PC_{61}BM$ has also been introduced into the perovskite layer as an additive to construct bulk-heterojunction (BHJ) PSCs. In 2015, Sargent *et al.* first reported that $PC_{61}BM$ as an additive was added into the perovskite precursor to construct regular-structure (n–i–p) bulk-heterojunction PSCs. Since the molecular size of $PC_{61}BM$ is large, the possibility of becoming interstitial species within the $CH_3NH_3PbI_3$ perovskite layer can be precluded, therefore $PC_{61}BM$ addition leads to homogeneous distribution at the grain boundaries within the perovskite layer. The rich-assembly of $PC_{61}BM$ at the grain boundaries is beneficial to passivate the iodide-rich trap sites (PbI_3^- antisite defects) through the formation of a $PC_{61}BM$-halide radical (Fig. 3c), resulting in reduced anion migration and suppressed current–voltage hysteresis of PSCs.[28] The conception of BHJ-PSCs *via* $PC_{61}BM$ was further testified by Gong and co-workers in 2015. BHJ-PSCs formed *via* adding $PC_{61}BM$ into the $CH_3NH_3PbI_3$ perovskite precursor afforded an improvement in PCE from 6.9% to 12.78% owing to the improved perovskite crystallinity and enhanced "donor/acceptor" interfaces of the perovskite and $PC_{61}BM$.[41] One year later, Wu and coworkers reported a two-step spin-coating method to construct $CH_3NH_3PbI_3$-$PC_{61}BM$ p–i–n BHJ-PSCs, revealing that $PC_{61}BM$ filled at the grain boundaries and vacancies of the perovskite films (Fig. 3d). The as-prepared p–i–n $CH_3NH_3PbI_3$ BHJ-PSCs delivered an improved PCE of 16.0% with an outstanding fill factor of 0.82 and no photocurrent hysteresis, attributed to the long charge diffusion length, balanced electron and hole mobilities and higher conductivity of the perovskite-$PC_{61}BM$ BHJ film.[42]

In addition to improving the device efficiency, constructing BHJ perovskite layers *via* $PC_{61}BM$ additives is also beneficial to enhance the thermal stability of PSC devices. In 2017, Cho and co-workers fabricated inverted $CH_3NH_3PbI_{3-x}Cl_x$ BHJ-PSCs with $PC_{61}BM$ as an additive, unveiling that $PC_{61}BM$ located at perovskite grain boundaries markedly improved the thermal stability of the devices and suppressed the decomposition of the perovskite. This was due to the decreased grain interface area and the impeded migration of the halogen ions within the perovskite lattice through electron transfer from the halogen ions to $PC_{61}BM$.[43] In 2016, Han *et al.* constructed a perovskite-fullerene graded heterojunction (GHJ) by dripping $PC_{61}BM$ dissolved in the anti-solvent toluene onto the upper formamidinium (FA) cation-containing perovskite layer, achieving a certified efficiency of 18.21% with a large area of 1.022 cm^2 (Fig. 3e).[44]

Considering the superior performance of $PC_{61}BM$ as a mono-adduct in PSCs, an intriguing question is whether the bis-adduct of $PC_{61}BM$ performs better or not. In 2017, Grätzel and co-workers incorporated isomer-pure bis-$PC_{61}BM$ (α-bis-$PC_{61}BM$, Fig. 2) into a $CH_3NH_3PbI_3$ perovskite film *via* an anti-solvent method, and found that α-bis-$PC_{61}BM$ could act as a templating agent for enhancing the crystallinity of perovskite films, leading to a PCE of 20.8% for n–i–p BHJ-PSCs, which is improved relative to that based on $PC_{61}BM$ (19.9%). Besides, due to the increased hydrophobicity and crystallinity of the perovskite film induced by α-bis-$PC_{61}BM$, the device achieves a remarkable improvement of stability relative to that of $PC_{61}BM$-based devices.[45]

The effect of the end alkyl group within $PC_{61}BM$ on its performance has also been investigated. A series of $PC_{61}BM$ analogues containing different end alkyl groups were synthesized and applied as ETLs by Bolink and co-workers so as to evaluate their hole blocking/electron transporting abilities for inverted $CH_3NH_3PbI_3$ PSCs, revealing that the longer alkyl groups help to reduce the defects within fullerene layers.[46] A more in-depth investigation on the influence of $PC_{61}BM$-analogues (Fig. 2) and $C_{60}MC_{12}$ (see Fig. 15) ETLs on the performance of inverted $CH_3NH_3PbI_{3-x}Br_x$ PSCs was performed by Miyano and co-workers in 2018, showing that fullerene derivatives with suitable energy level and crystallinity regulation *via* alkyl length contribute to the improved device efficiency.[47] More recently, four $PC_{61}BM$-like fullerene derivatives F1–F4 (Fig. 2) were applied by Troshin and co-workers as ETLs in inverted $CH_3NH_3PbI_3$ PSCs, among which devices based on F1 containing *n*-propyl show the best ambient stability. The outstanding performance of the F1 ETL is due to the optimal alkyl length enabling the side chains to fill the gaps between fullerene spheres for preventing the diffusion of oxygen and moisture into the devices.[48]

Echegoyen and co-workers reported a novel $PC_{61}BM$-analogue $PC_{61}BEH$ (Fig. 2) with a branched alkyl chain in 2018, which was applied as an ETL of inverted $CH_3NH_3PbI_3$ PSCs, achieving an improved PCE relative to that of the control device based on the $PC_{61}BM$ ETL. Such an improved performance was attributed to the improved film morphology, enhanced defect passivation and electron extraction ability *via* the branched alkyl group.[49] Likewise, a series of mono-, bis- and tris-benzene octyl ether functionalized fullerene derivatives (PCBOEs, Fig. 2) were also synthesized and applied as ETLs in p–i–n $CH_3NH_3PbI_3$ PSCs as well. Increasing the number of adducts further decreases the electron mobility of PCBOEs which leads to charge accumulation at the perovskite/ETL interface, delivering a lower PCE than that of the $PC_{61}BM$ ETL.[50] In addition to the alkyl groups, Jen and co-workers synthesized a series of donor–acceptor fullerene derivatives by grafting triphenylamine (TPA) (Fig. 3f) onto the C_{60} cage, and applied them as ETLs of inverted p–i–n $CH_3NH_3PbI_{3-x}Cl_x$ PSCs. The intramolecular charge transfer from TPA to C_{60} helps to

improve molecular polarization, carrier density, and charge transport/excitation capability, contributing to the improved device performance.[51]

Expect for the ETL, another role of $PC_{61}BM$ is to serve as a cathode modification layer to improve the performance of n–i–p PSCs.[52] A triblock fullerene derivative (PCBB-2CN-2C8, Fig. 2) was designed and synthesized by Yang and co-workers, which was applied as a cathode modification layer atop the TiO_2 ETL of the regular n–i–p $CH_3NH_3PbI_3$ PSCs. The rationally designed molecular structure of PCBB-2CN-2C8 fulfils multiple functions including: (a) the C_{60} moiety possesses high electron affinity for efficient electron extraction and transfer; (b) the electron-deficient cyano-groups could passivate the oxygen vacancy of TiO_2 for decreasing the interface recombination; (c) the grafted dioctyloxy chains and cyano-groups on the fullerene cage were able to reduce the solubility of PCBB-2CN-2C8 in polar solvents, which is beneficial for orthogonal solution-processing. As a result PCBB-2CN-2C8 incorporation led to an improved PCE from 14.38% to 17.35% as well as suppressed hysteresis.[53]

Table 1 provides an exhaustive list of all reported $PC_{61}BM$ and $PC_{61}BM$-based fullerene derivatives applied in PSCs. Although $PC_{71}BM$ may deliver a comparable device performance with the $PC_{61}BM$ ETL in p–i–n PSCs, the traditional chemical reaction may inevitably occur at different reactive sites of C_{70} to afford a mixture of multiple isomers of $PC_{71}BM$, and the blending ratio of these isomers would influence the device performance obviously. Therefore, based on these results, it is clearly shown that $PC_{61}BM$ is the most commonly used fullerene derivative, which plays three versatile roles including as an independent ETL, an interfacial modifier and an additive in either p–i–n or n–i–p PSCs. Tailoring the end alkyl groups appears to impose little effect on the LUMO energy level of the fullerene derivative, while involving donor group acceptors such as triphenylamine can increase the LUMO energy level. Using bis-adducts of fullerene is another effective approach to raise the LUMO energy levels relative to that of monoadducts, leading to a better matching of energy level alignment, consequently facilitating charge transfer and affording a higher V_{oc}. Hence, considering the complex synthetic procedure and high cost of $PC_{61}BM$, developing novel fullerene derivatives *via* grafting other functional groups as alternatives to achieve higher device performance of PSCs is highly desirable.[6,54]

3. Lewis base functionalized fullerene derivatives

Unlike the $PC_{61}BM$ bearing ester groups and alkyl chains, grafting electron-rich groups (*i.e.*, Lewis bases) onto the fullerene cage leads to enhanced polarity for fullerene derivatives, rendering different mechanisms upon being applied in PSCs. So far the reported Lewis bases include amine, oligoether, crown-ether and heterocycles *etc.*

3.1 Amino-functionalized fullerene derivatives

Amino groups as a representative Lewis base were extensively used to functionalize fullerenes. The reported amino groups include an amino ($-NH_2$) group, a dimethylamino ($-N(CH_3)_2$) group and trimethylamine halide ($-N^+(CH_3)_3I^-$) ions, which were grafted onto the fullerene cage contributing to the formation of an Ohmic contact between the metal/perovskite interface by lowering the work function of the metal electrode. In addition, the strong electric dipole feature of amino-functionalized fullerene derivatives helps to form interfacial dipole layers, which are beneficial for forming built-in electric

Table 1 An exhaustive list of all reported $PC_{61}BM$ and $PC_{61}BM$-based fullerene derivatives applied in PSCs

Compound	Active layer	LUMO[a] (eV)	μ[b] ($cm^2\ V^{-1}\ s^{-1}$)	Role of the molecule	J_{sc} ($mA\ cm^{-2}$)	V_{oc} (V)	FF (%)	PCE (%)	Ref.
$PC_{61}BM$	$CH_3NH_3PbI_3$	−3.9	—	ETL	10.32	0.60	63	3.9	33
$PC_{61}BM$	$CH_3NH_3PbI_3$	−3.9	—	ETL	22.6	1.13	75.0	19.4	35
$PC_{61}BM$	$CH_3NH_3PbI_3$	—	—	Additive	18.0	1.086	75	14.4	28
$PC_{61}BM$	$CH_3NH_3PbI_3$	—	—	Additive	20.2	0.97	82	16.0	42
$PC_{61}BM$	$FA_{0.85}MA_{0.15}Pb(I_{0.85}Br_{0.85})_3$	—	—	Additive	21.98	1.08	79	18.75	44
$PC_{71}BM$	$CH_3NH_3PbI_3$	—	—	ETL	19.98	1.05	78	16.31	39
α-Bis-$PC_{61}BM$	$CH_3NH_3PbI_3$	—	—	Additive	23.95	1.13	74	20.8	45
PCBB	$CH_3NH_3PbI_3$	−3.91	—	ETL	16.02	1.09	76	13.27	46
PCBH	$CH_3NH_3PbI_3$	−3.91	—	ETL	15.92	1.10	79	13.75	46
PCBB	$CH_3NH_3PbI_{3-x}Br_x$	−4.12	—	ETL	16.68	1.12	78	14.82	47
PCBO	$CH_3NH_3PbI_{3-x}Br_x$	−4.12	—	ETL	16.52	1.12	78	14.37	47
PCBD	$CH_3NH_3PbI_{3-x}Br_x$	−4.12	—	ETL	16.75	1.11	51	9.44	47
F1	$CH_3NH_3PbI_3$	—	—	ETL	18.3	0.93	73	11.4	48
F2	$CH_3NH_3PbI_3$	—	—	ETL	18.9	0.91	74	12.3	48
F3	$CH_3NH_3PbI_3$	—	—	ETL	19.1	0.93	74	13.0	48
F4	$CH_3NH_3PbI_3$	—	—	ETL	20.6	0.90	79	14.6	48
$PC_{61}BEH$	$CH_3NH_3PbI_3$	−3.89	4.76×10^{-4}	ETL	22.5	0.95	77.61	16.26	49
Mono-PCBEOE	$CH_3NH_3PbI_3$	−3.74	8.8×10^{-4}	ETL	10.30	1.04	44.04	4.72	50
Bis-PCBOE	$CH_3NH_3PbI_3$	−3.65	2.6×10^{-4}	ETL	2.13	1.03	65.98	1.39	50
Tris-PCBOE	$CH_3NH_3PbI_3$	−3.56	2.7×10^{-4}	ETL	1.71	1.03	74.32	1.31	50
TPA-PCBM	$CH_3NH_3PbI_{3-x}Cl_x$	−3.69	7.9×10^{-4}	ETL	10.87	0.88	69	17.71	51
BrTPA-PCBM	$CH_3NH_3PbI_{3-x}Cl_x$	−3.70	3.3×10^{-4}	ETL	10.20	0.89	67	17.18	51
CNTPA-PCBM	$CH_3NH_3PbI_{3-x}Cl_x$	−3.72	7.2×10^{-5}	ETL	5.60	0.90	48	13.76	51
PCBB-2CN-2C8	$CH_3NH_3PbI_3$	−4.01	4.8×10^{-3}	Modifying TiO_2	20.68	1.06	79.1	17.35	53

[a] LUMO means the lowest unoccupied molecular orbital energy level. [b] μ is the electron mobility.

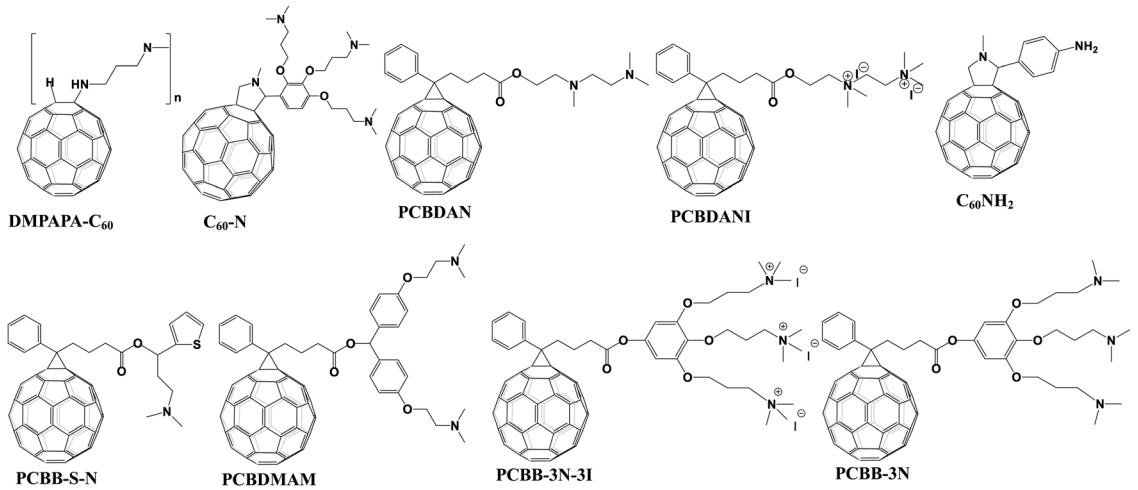

Fig. 4 Molecular structures of amine functionalized fullerene derivatives applied in PSCs.

field and enhancing charge collection.[6,26] In 2015, Azimi *et al.* synthesized a novel dimethylamino-containing fullerene derivative DMAPA-C_{60} (Fig. 4) and applied it as a cathode buffer layer (CBL) modifying the $PC_{61}BM$ layer of p–i–n $CH_3NH_3PbI_{3-x}Cl_x$ PSCs, achieving a PCE of 13.4% which was higher than that of the control device without the CBL (9.4%). The improved PCE after introducing the DMAPA-C_{60} CBL was attributed to the formation of the interfacial dipole layer between $PC_{61}BM$ and the Ag electrode. This resulted in the quasi-ohmic contact between the $PC_{61}BM$ ETL and the Ag electrode, the reduced work function of the Ag electrode as well as the minimized interfacial energy barrier.[55] Later on, Russell *et al.* reported that incorporating C_{60}–N containing three dimethylamino groups (Fig. 4) as an interlayer between the $PC_{61}BM$ ETL and the Ag electrode of inverted $CH_3NH_3PbI_3$ PSCs offered a PCE of 15.5%, which was higher than that of the control device without C_{60}–N (7.5%). The incorporated C_{60}–N interlayer enabled the lowered work function of the Ag electrode, the reduced combination loss and longer lifetime of free carriers *via* the optimized interface, contributing to the improved device performance.[56] In the same year, Yang *et al.* synthesized another dimethylamino-containing fullerene derivative (PCBDAN, Fig. 4), which was applied as a CBL sandwiched between the $PC_{61}BM$ ETL and the Ag electrode in inverted PSCs, affording a PCE of 17.2% with a negligible hysteresis. The PCBDAN interlayer facilitated the decrease of the interface barrier and protected the $CH_3NH_3PbI_3$ perovskite film from the corrosion of moisture.[57] In addition to the application as a CBL, Yang *et al.* further applied PCBDAN as the modification layer of the TiO_2 ETL in planar n–i–p PSCs, achieving improvement of PCE from 13.64% to 16.78% with enhanced light soaking stability. PCBDAN led to a smoother surface and a larger grain size of the $CH_3NH_3PbI_3$ perovskite film, a reduced interfacial barrier and a suppressed photocatalytic capability of TiO_2.[58] One year later, the same group further prepared a self-organized PCBDAN interlayer sandwiched between the ITO electrode and the $PC_{61}BM$ ETL, obtaining a PCE of 18.1% with almost free hysteresis and excellent stability maintaining 85% of its initial PCE after 240 h under UV-light soaking. The improved device performance was attributed to the reduced work function of ITO and minimized interface barriers between the $PC_{61}BM$ ETL and the ITO electrode through the self-organized PCBDAN interlayer.[59] Interestingly, PCBDAN can be further ionized by methyl iodide, resulting in a novel methanol-soluble fullerene derivative (PCBDANI, Fig. 4), which was later applied as a CBL in p–i–n $CH_3NH_3PbI_{3-x}Cl_x$ PSCs by Li *et al.* After incorporating the PCBDANI CBL, PSCs exhibited the best PCE of 15.71%, which is attributed to the decreased interfacial recombination derived from the formed interfacial dipole between the $PC_{61}BM$ ETL and the Al electrode.[60] Very recently, our group synthesized a novel bis-dimethylamino-functionalized fullerene derivative (PCBDMAM, Fig. 4), which was deposited atop $PC_{61}BM$ to construct $PC_{61}BM$/PCBDMAM double fullerene CBLs of p–i–n $CH_3NH_3PbI_3$ PSCs. The devices based on $PC_{61}BM$/PCBDMAM double fullerene CBLs achieved the highest PCE of 18.11% and enhanced ambient stability, owing to the decreased interfacial energy offset between $PC_{61}BM$ and the Ag electrode *via* the reduced work function of the Ag cathode (Fig. 5a).[61]

In addition to the work function modulation of the corresponding metal electrode, amino-functionalized fullerene derivatives can play another important role in defect passivation and interfacial energy band reconstruction. Recently, Xiang *et al.* developed a simple amino-modified fullerene derivative ($C_{60}NH_2$, Fig. 4) and applied it as an interfacial modifier of the TiO_2 ETL in regular planar PSCs, affording an improved PCE of 18.34% and suppressed hysteresis. The $C_{60}NH_2$ interfacial layer helped to improve crystallinity of the $CH_3NH_3PbI_3$ perovskite and the electronic interaction between $C_{60}NH_2$ and the TiO_2 layer, resulting in enhanced photogenerated carrier extraction and reduced interfacial recombination between TiO_2 and the perovskite layer.[62] On the other hand, Li *et al.* synthesized a novel fullerene derivative (PCBB-S-N, Fig. 4) bearing thiophene and amino groups, and applied PCBB-S-N as an intermediary layer atop the $CH_3NH_3PbI_3$ perovskite. The inverted PSCs with a PCBB-S-N interlayer delivered the best PCE of 21.08% and excellent ambient/thermal stability without any encapsulation. Due to the coordination interaction between the thiophene

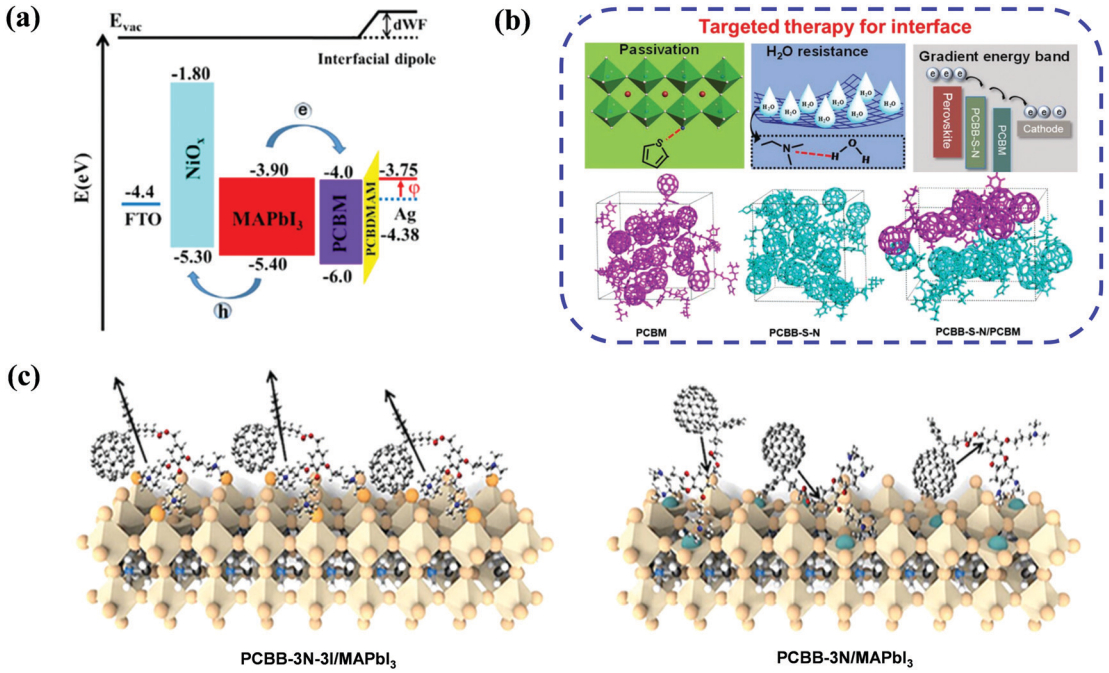

Fig. 5 (a) Schematic diagram of iPSCs with a CBL and the cathode interaction process. The energy-level diagram of the iPSCs. Reproduced with permission from ref. 61. Copyright 2020, Elsevier B.V. (b) Functions of PCBB-S-N and three configurations of molecular mutual positions at the end of MD simulation performed under periodic boundary conditions. Reproduced with permission from ref. 63. Copyright 2019, Wiley-VCH. (c) Schematic illustration of the molecular orientation of PCBB-3N-3I and PCBB-3N. Reproduced with permission from ref. 64. Copyright 2019, Nature Publishing Group.

group and Pb^{2+} ions as well as the hydrogen bond interaction between the amino moiety and H_2O, the PCBB-S-N interlayer helped to form a compact and homogeneous $PC_{61}BM$ film and regulated the enlarged band energy offset between the perovskite layer and the $PC_{61}BM$ ETL, which is beneficial to enhance the electron transfer capability. Accordingly, they named such interfacial engineering as a targeted therapy strategy (Fig. 5b).[63] Furthermore, in order to eliminate the charged defects at the surface of the organic–inorganic perovskite layer which is detrimental to charge transport, the same group inserted an iodide ionized fullerene derivative (PCBB-3N-3I) between $PC_{61}BM$ and perovskite to construct planar p–i–n $CH_3NH_3PbI_3$ PSCs, achieving a high PCE of 21.1% and robust ambient stability which was superior to that of the control device (17.70%) and the device with PCBB-3N (15.77%, Fig. 4). PCBB-3N-3I was unveiled to bind the positively charged defects on the perovskite surface *via* electrostatic interaction, which was beneficial for passivating trap states and forming an assembled dipole interlayer atop the perovskite film, leading to an optimized interfacial energy band structure and an extra built-in field for charge collection (Fig. 5c).[64]

3.2 Oligoether and crown-ether functionalized fullerene derivatives

In addition to the amino groups, other polar Lewis bases such as oligoether and crown-ether were also used to develop novel fullerene derivatives applied in PSCs. In 2014, Jen *et al.* synthesized a novel fullerene derivative (bis-C_{60}, Fig. 6) and applied it as an efficient CBL sandwiched between $PC_{61}BM$ and the Ag electrode in planar p–i–n PSCs. The incorporation of bis-C_{60} helped to align the energy levels between the $PC_{61}BM$ ETL and the Ag electrode. As a result, $CH_3NH_3PbI_{3-x}Cl_x$ PSCs with a bis-C_{60} interlayer and 1,8-diiodooctane as the auxiliary additive of the perovskite afforded the PCE of 11.8%.[65] In 2018, Li *et al.* used Bis-FIMG and Bis-FITG (Fig. 6) as a CBL atop $PC_{61}BM$ in inverted planar $CH_3NH_3PbI_3$ p–i–n PSCs, achieving PCEs of 19.31% and 19.01%, respectively, both higher than that of the control device with a BCP CBL (18.8%). Such ionic fullerene derivatives act as surfactants with suitable conductivity, capable of tuning the work function and orthogonal solution-processing.[66]

In 2016, Loi *et al.* prepared a fulleropyrrolidine with a triethylene glycol monoethyl ether side chain (PTEG-1, Fig. 6) and used it as an electron extraction layer (EEL) of planar p–i–n $CH_3NH_3PbI_{3-x}Cl_x$ PSCs. Compared to the control device with $PC_{61}BM$ EEL suffering from serious light soaking, the devices based on PTEG-1 EEL exhibited negligible light soaking effect and improved PCE of 15.7%. The superior performance of PTEG-1 EEL was due to its higher dielectric constant (5.9) than that of $PC_{61}BM$ (3.9) and the suppressed trap-assisted recombination resulted from the electron donating side chain groups (Fig. 7a).[67] Likewise, Cao *et al.* synthesized a series of hydrophilic fullerene derivatives bearing electron-rich oligoether chains (Fig. 7b) and applied them as alternative ETLs to replace the $PC_{61}BM$ ETL in inverted planar PSCs. The influences of addition patterns (monoadducts or bisadduct), the number of oligoether chains and the type of fullerenes (C_{60} and C_{70}) on the ETL performance were elucidated, and PSCs based on C_{70}-DPM-OE

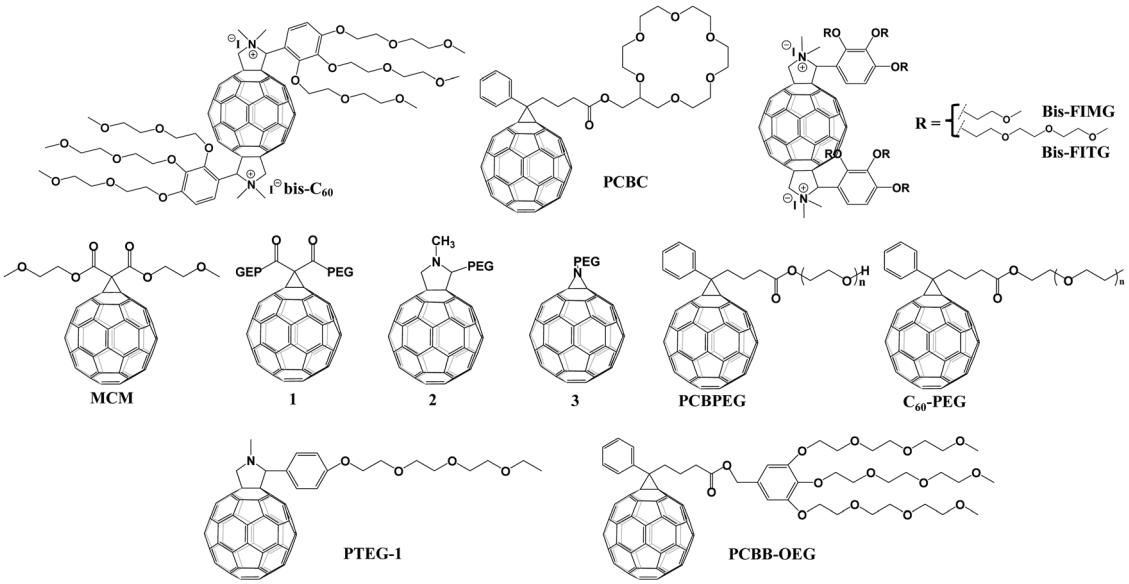

Fig. 6 Molecular structures of oligoether and crown-ether functionalized fullerene derivatives applied in PSCs.

with the optimized molecular structures exhibited the highest PCE of 16%. The electron-rich oligoether chains within C_{70}-DPM-OE enable the enhanced interfacial charge transport efficiency, the modified work function of Ag cathodes and the passivated trap states at the $CH_3NH_3PbI_{3-x}Cl_x$ perovskite surface.[68] In 2012, two novel fullerene derivatives including MCM bearing an oligoether group (Fig. 6) and PCP bearing a pyridine moiety (Fig. 8) were synthesized *via* Bingel reactions and applied as ETLs in thick-film $CH_3NH_3PbI_3$ PSCs (absorber layer $>$ 1 μm) by Li *et al.*, affording a PCE of 19.11% and 19.32%, respectively. Comparing these two ETMs, the authors proposed that the subtle intermolecular interaction (anion–π and Lewis acid–base) between the ETL and the perovskite determines the carrier extraction and transport at the interface between the perovskite and the cathode, which are correlated to the device hysteresis and performance. Furthermore, this study points out that the stronger coordination interaction of the N atom and Pb^{2+} (N–Pb^{2+}) than that of O–Pb^{2+} results in serious hysteresis owing to the energetic misalignment as well as the charge accumulation at the perovskite/PCP heterojunction.[69]

In 2018, Li *et al.* grafted tri-hydrophilic OEG chains onto the fullerene cage and applied the as-synthesized PCBB-OEG (Fig. 6) as an additive in the MAI precursor solution to prepare p–i–n planar PSCs by the two-step deposition method.[70] PCBB-OEG in the MAI solution acts as a soft-template to assist the growth of high-quality $CH_3NH_3PbI_3$ crystals through diffusion into the pre-deposited PbI_2:MAI film, resulting in a top-down gradient distribution of the fullerene derivative in the perovskite film, which is beneficial for improving electronic coupling

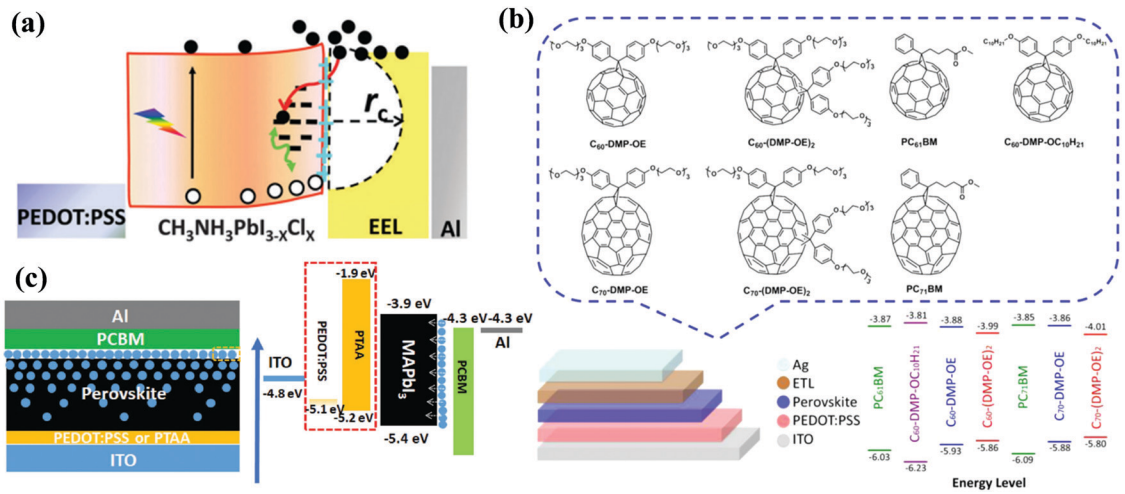

Fig. 7 (a) Proposed mechanism for the light-soaking effect for the device with $PC_{61}BM$ and PTEG-1. Reproduced with permission from ref. 67. Copyright 2016, Royal Society of Chemistry. (b) Chemical structure of fullerene derivatives and the corresponding energy-level diagram. Reproduced with permission from ref. 68. Copyright 2016, Elsevier Ltd. (c) Device configuration and the corresponding energy-level diagram of the PSCs. Reproduced with permission from ref. 70. Copyright 2018, Wiley-VCH.

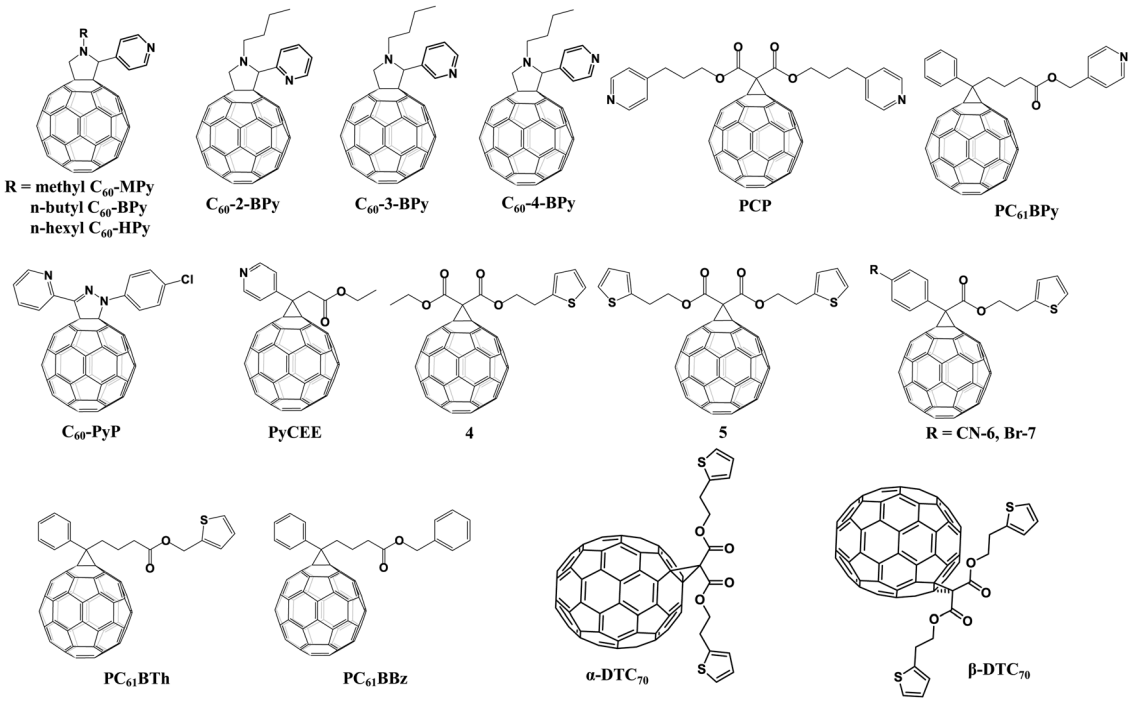

Fig. 8 Molecular structures of heterocyclic functionalized fullerene derivatives applied in PSCs.

and band alignment at the interface and reducing the trap-states at the perovskite grain boundaries (Fig. 7c). These advantages contribute to an enhanced PCE of 20.2% for a rigid device on a glass substrate and a PCE of 18.1% for the flexible PSCs without hysteresis. Besides, the anchoring of PCBB-OEG with perovskite *via* the hydrogen bond interaction between –O of –OEG and $–NH_3$ of MA, as well as the outside orientation of C_{60} moieties at the perovskite surface, simultaneously contribute to the enhancements of the stability of the perovskite crystal lattice and water resistance. As a result, PSCs with the PCBB-OEG additive demonstrate an outstanding ambient stability maintaining more than 98.4% of the initial PCE after storing the device under ≈50–70% RH after 300 h without any encapsulation. In 2019, the same group further carried out an in-depth investigation of the mechanism toward the oxygen-stabilizing effect of PCBB-OEG doping both in the perovskite active layer and in the $PC_{61}BM$ ETL.[71] The PCBB-OEG additive in the perovskite and the $PC_{61}BM$ ETL enhanced electron extraction and transport capability from $CH_3NH_3PbI_3$ to the PCBB-OEG/$PC_{61}BM$ layer, preventing the formation of $O_2^{\bullet-}$ from the photogenerated charge reaction with oxygen which is responsible for device degradation.[71]

In 2015, Li *et al.* reported a new alcohol-soluble crown-ether-containing fullerene derivative (PCBC, Fig. 6) and applied it as a CBL between $PC_{61}BM$ and the Al electrode in inverted planar $CH_3NH_3PbI_{3-x}Cl_x$ PSCs. The incorporated PCBC CBL improved the interfacial Ohmic contact between $PC_{61}BM$ and Al and lowered the interfacial resistance, which is beneficial for electron extraction and transport, resulting in an improved PCE of 15.08%.[72] Soon after, Li *et al.* deposited a LiF interlayer atop of PCBC to construct the PCBC/LiF double CBL of planar p–i–n $CH_3NH_3PbI_{3-x}Cl_x$ PSCs, affording a PCE of 15.53%, which is higher than that of the control device with only LiF CBL (13.54%). Furthermore, the devices with the PCBC/LiF double CBL demonstrate superior long-term stability to that of the control device with a LiF single CBL. The enhanced performance is attributed to the reduced series resistance (R_s) from the better Ohmic contact between $PC_{61}BM$ and the LiF/Al electrode induced by the dipole moment of PCBC.[73]

In 2018, Delgado *et al.* presented three kinds of poly(ethylene glycol) (PEG) functionalized fullerene derivatives (**1**, **2**, **3**, Fig. 6) and incorporated them as additives in the $CH_3NH_3PbI_3$ perovskite layer of regular PSCs, showing a suppressed hysteresis and increased moisture stability. They found that increasing the number of PEG moieties led to the enhanced device stability, and it was interpreted that the increased hygroscopicity of PEG chains was beneficial for retaining water, thus preventing the perovskite from degrading.[74] Similarly, Wu *et al.* developed two PEG end-capped fullerene derivatives (PCBPEG-4k and PCBPEG-20k, Fig. 6) and applied them as additives in the $CH_3NH_3PbI_3$ perovskite layer of planar regular PSCs, affording a PCE of 17.72% and 17.36%, respectively. Incorporating PCBPEG-4k and PCBPEG-20k additives into the perovskite layer improved the perovskite morphology and photovoltaic performance of the device, which is due to the enlarged crystal grain size, reduced defect density and improved charge transfer properties.[75] Later on, Hu *et al.* reported another similar PEG end-capped fullerene derivative (C_{60}-PEG, Fig. 6), which was incorporated as an additive into the $Cs_{0.1}FA_{0.7}MA_{0.2}I_{3-x}Br_x$ perovskite layer in planar inverted PSCs *via* the anti-solvent process. The incorporation of C_{60}-PEG enlarges the perovskite crystal size and passivates the defects of the perovskite film, leading to higher electron mobility and

lower carrier recombination as well as the increased PCE of 17.71%.[76]

3.3 Heterocyclic pyridine and thiophene functionalized fullerene derivatives

Pyridine and thiophene are two representative heterocyclic groups and common Lewis bases which are used to regulate the crystallization of perovskite and passivate the trap states through the strong coordination interactions between Pb^{2+} ions and nitrogen/sulfur atoms bearing lone pair electrons.[77] In 2019, our group first grafted the pyridine group onto C_{60} and synthesized three novel pyridine-functionalized fullerene derivatives with different alkyl groups (methyl, *n*-butyl, and *n*-hexyl, abbreviated as C_{60}-MPy, C_{60}-BPy, and C_{60}-HPy respectively, Fig. 8) *via* a one-step 1,3-dipolar cycloaddition reaction (*i.e.*, Prato reaction), and applied them as ETLs in p–i–n PSCs.[78] The pyridine moiety within C_{60}-Py can coordinate with Pb^{2+} ions of $CH_3NH_3PbI_3$ to passivate the trap states and suppress the nonradioactive recombination, leading to the improved electron transfer and device performance. The PCE based on the C_{60}-BPy ETL demonstrated the highest PCE of 16.83%, which is higher than that of the control device based on the $PC_{61}BM$ ETL (15.87%). In addition, the longest *N*-alkyl group could act as an encapsulating layer protecting the perovskite film from the erosion of moisture, thus improving the ambient stability of PSC devices.[78] Furthermore, very recently we carried out a follow-up study on the effect of the nitrogen site on the ETL performance of C_{60}-BPy based on syntheses of three pyridine-functionalized fullerene derivatives with different nitrogen sites abbreviated as C_{60}-*n*-Py (*n* = 2, 3, 4, Fig. 8). Interestingly, after incorporating C_{60}-*n*-Py as ETLs in p–i–n PSCs, it was found that C_{60}-3-Py with the optimal nitrogen site fulfilled the strongest coordination interactions with Pb^{2+} ions and consequently passivated the $CH_3NH_3PbI_3$ perovskite defects at the most. As a result, C_{60}-3-Py-based PSC devices achieved the highest PCE of 17.57% (Fig. 9a).[79]

Another pyridine-functionalized fullerene derivative PCP (Fig. 8) was synthesized by Li *et al. via* the Bingel reaction and applied as the ETL in p–i–n PSCs, leading to an improved PCE of 19.32%.[69] In 2019, Deng and Xie *et al.* synthesized a novel pyridine-functionalized fullerene derivative (PyCEE, Fig. 8) and applied it as an alternative of the traditional TiO_2 ETL to construct planar n–i–p PSCs. Compared with TiO_2, the PyCEE ETL possesses a poor-wetting surface, more suitable energy levels, higher electron mobility and stronger trap passivation capability by the coordination interactions with Pb^{2+} within the $CH_3NH_3PbI_3$ film, leading to large-sized perovskite films, higher electron extraction/transport ability, suppressed hysteresis and the champion PCE of 18.27% (Fig. 9b).[80]

A series of thiophene-grafted fullerene derivatives (**4–7**, Fig. 8) were synthesized by Bingel reactions and applied as novel ETLs in inverted $CH_3NH_3PbI_3$ PSCs by Echegoyen and co-workers. Compared with $PC_{61}BM$ ETLs, PSCs with these new thiophene-grafted fullerene derivative ETLs exhibited improved PCE, owing to the passivation of the defects of the perovskite surface by the coordination interactions between Pb and S atoms. Interestingly, among the three fullerene derivatives, devices based on fullerene derivatives bearing highly polar –CN groups exhibited the highest PCE of 17.77% due to the increased dielectric constant (ε_r), which could decrease the recombination ratio and facilitate the charge transfer.[81] More recently, the same group prepared

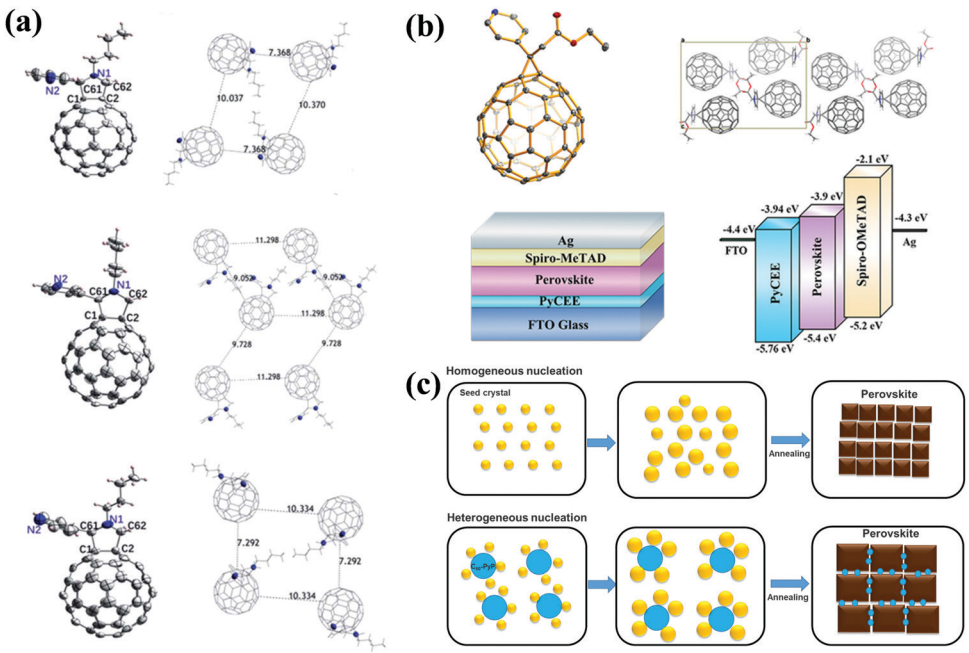

Fig. 9 (a) Crystal structure and the corresponding molecular packing of C_{60}-*n*-Py (*n* = 2, 3, 4). Reproduced with permission from ref. 79. Copyright 2020, Royal Society of Chemistry. (b) Crystal structure, the corresponding molecular packing of PyCEE, and the energy-level diagram of the PSCs. Reproduced with permission from ref. 80. Copyright 2019, American Chemical Society. (c) Schematic illustration of the perovskite nucleation process without and with C_{60}-PyP. Reproduced with permission from ref. 27. Copyright 2019, Royal Society of Chemistry.

another thiophene-grafted fullerene derivative $PC_{61}BTh$ and compared its performance with the analogous derivatives $PC_{61}BBz$ and $PC_{61}BPy$ (Fig. 8) bearing, respectively, benzyl and pyridine as the end groups so as to investigate the influence of the heterocyclic groups on the photovoltaic performance and interfacial interactions. Among them, $PC_{61}BPy$ with a pyridine group exhibited the strongest interfacial interactions with Pb^{2+} ions of the $CH_3NH_3PbI_3$ perovskite surface, which leads to more effective trap passivation and decreased electron/hole recombination, and consequently the best PCE of 17.84%.[82] Very recently, they further synthesized two new thiophene substituted C_{70} isomers, α and β bis(2-(thiophen-2-yl)ethyl)-C_{70}-fullerene monoadducts (α-DTC_{70} and β-DTC_{70}, Fig. 8), which were applied as ETLs in inverted $CH_3NH_3PbI_3$ PSCs. They found that, compared with the original fullerene, the change in the orientation of fullerene is due to the carbonyl-lead interaction that fixes the fullerene on the surface of the perovskite, and the shortest contacts between α-DTC_{70} and the perovskite afforded an improved electron extraction ability, leading to improved J_{sc} and FF of the devices with a PCE of 15.9%, which is higher than those of the traditional $PC_{71}BM$ ETL (15.1%) and β-DTC_{70} ETL (8.80%).[83]

In addition to the applications as ETLs in PSCs, incorporating these heterocyclic pyridine and thiophene fullerene derivatives into the perovskite layer as additives to construct BHJ-PSCs is another effective way to improve device performance. In 2019, our group synthesized a pyridine-functionalized fullerene derivative (C_{60}-PyP, Fig. 8) and applied it as an additive of the $CH_3NH_3PbI_3$ perovskite film in p–i–n PSCs. The incorporation of C_{60}-PyP additives into the perovskite led to lowering of the

Table 2 Device performance of PSCs incorporating amine, oligoether and crown-ether functionalized fullerene derivatives

Compound	Active layer	LUMO (eV)	μ ($cm^2\ V^{-1}\ s^{-1}$)	Role of the molecule	J_{sc} (mA cm^{-2})	V_{oc} (V)	FF (%)	PCE (%)	Ref.
DMPAPA-C_{60}	$CH_3NH_3PbI_{3-x}Cl_x$	—	—	CBL	17.90	0.97	77	13.40	55
C_{60}–N	$CH_3NH_3PbI_3$	−3.9	—	CBL	20.50	1.03	74	15.50	56
PCBDAN	$CH_3NH_3PbI_3$	−4.1	—	CBL	20.71	1.08	77.00	17.20	57
PCBDAN	$CH_3NH_3PbI_3$	−4.1	—	Modifying TiO_2	21.3	1.05	75.05	16.78	58
PCBDAN	$CH_3NH_3PbI_3$	−4.1	—	Interfacial layer	21.70	1.08	77.3	18.1	59
PCBDANI	$CH_3NH_3PbI_{3-x}Cl_x$	−3.68	—	CBL	21.28	0.91	81.00	15.71	60
PCBDMAM	$CH_3NH_3PbI_3$	—	1.08×10^{-4}	CBL	22.20	1.034	78.87	18.11	61
$C_{60}NH_2$	$CH_3NH_3PbI_3$	—	—	Modifying TiO_2	22.52	1.07	77	18.34	62
PCBB-S-N	$CH_3NH_3PbI_3$	−4.0	3.37×10^{-4}	Intermediary layer	23.83	1.12	79.09	21.08	63
PCBB-3N	$CH_3NH_3PbI_3$	−3.62	2.90×10^{-4}	Intermediary layer	21.05	1.046	71.65	15.77	64
PCBB-3N-3I	$CH_3NH_3PbI_3$	−3.66	9.24×10^{-4}	Intermediary layer	23.46	1.105	81.36	21.10	64
Bis-C_{60}	$CH_3NH_3PbI_{3-x}Cl_x$	—	—	CBL	17.5	0.92	73	11.8	65
Bis-FIMG	$CH_3NH_3PbI_3$	−3.97	—	CBL	22.92	1.08	79.5	19.31	66
Bis-FITG	$CH_3NH_3PbI_3$	−3.99	—	CBL	22.15	1.07	80.4	19.01	66
PCBC	$CH_3NH_3PbI_{3-x}Cl_x$	—	—	CBL	22.08	0.98	70	15.08	72
PCBC	$CH_3NH_3PbI_{3-x}Cl_x$	—	—	CBL	21.54	1.00	72.5	15.53	73
PTEG-1	$CH_3NH_3PbI_{3-x}Cl_x$	—	—	ETL	20.63	0.94	81	15.71	67
C_{60}-DMP-OE	$CH_3NH_3PbI_{3-x}Cl_x$	−3.88	5.0×10^{-4}	ETL	21.4	0.96	76	15.5	68
C_{60}-$(DMP\text{-}OE)_2$	$CH_3NH_3PbI_{3-x}Cl_x$	−3.99	1.8×10^{-5}	ETL	20.7	0.93	71	13.8	68
C_{60}-DMP-$OCH_{10}H_{21}$	$CH_3NH_3PbI_{3-x}Cl_x$	−3.81	1.1×10^{-4}	ETL	19.9	0.90	60	10.8	68
C_{70}-DMP-OE	$CH_3NH_3PbI_{3-x}Cl_x$	−3.86	3.3×10^{-4}	ETL	21.9	0.97	75	16.0	68
C_{70}-$(DMP\text{-}OE)_2$	$CH_3NH_3PbI_{3-x}Cl_x$	−4.01	1.7×10^{-5}	ETL	21.0	0.94	71	14.0	68
MCM	$CH_3NH_3PbI_3$	−3.88	—	ETL	22.12	1.08	80	19.11	69
1	$CH_3NH_3PbI_3$	−3.72	—	Additive	20.7	1.09	73	16.41	74
2	$CH_3NH_3PbI_3$	−3.64	—	Additive	17.8	1.06	76	15.07	74
3	$CH_3NH_3PbI_3$	−3.69	—	Additive	18.5	1.07	78	16.37	74
PCBPEG-4k	$CH_3NH_3PbI_3$	—	—	Additive	21.28	1.073	77.62	17.72	75
PCBPEG-20k	$CH_3NH_3PbI_3$	—	—	Additive	21.21	1.074	76.17	17.36	75
C_{60}-PEG	$Cs_{0.1}FA_{0.7}MA_{0.2}I_{3-x}Br_x$	—	—	Additive	20.50	1.04	81.66	17.41	76
PCBB-OEG	$CH_3NH_3PbI_3$	—	—	Additive	23.65	1.07	80	20.2	70
C_{60}-MPy	$CH_3NH_3PbI_3$	−3.80	1.97×10^{-3}	ETL	20.2	1.016	78.4	16.1	78
C_{60}-Bpy	$CH_3NH_3PbI_3$	−3.81	3.51×10^{-3}	ETL	22.8	1.003	74.2	16.8	78
C_{60}-HPy	$CH_3NH_3PbI_3$	−3.83	1.04×10^{-3}	ETL	20.6	0.988	70.8	14.4	78
C_{60}-2-BPy	$CH_3NH_3PbI_3$	−3.78	1.02×10^{-3}	ETL	20.45	0.85	64.67	12.68	79
C_{60}-3-Bpy	$CH_3NH_3PbI_3$	−3.80	2.95×10^{-3}	ETL	22.46	1.02	76.42	17.57	79
C_{60}-4-BPy	$CH_3NH_3PbI_3$	−3.81	2.64×10^{-3}	ETL	22.85	1.00	74.20	16.83	79
PCP	$CH_3NH_3PbI_3$	−3.88	—	ETL	22.31	1.11	78	19.32	69
PyCEE	$CH_3NH_3PbI_3$	−3.94	—	ETL	22.95	1.05	75.83	18.27	80
4	$CH_3NH_3PbI_3$	−3.88	1.32×10^{-3}	ETL	21.00	0.93	82	16.01	81
5	$CH_3NH_3PbI_3$	−3.88	4.58×10^{-3}	ETL	22.10	0.94	83	17.22	81
6	$CH_3NH_3PbI_3$	−3.88	7.68×10^{-3}	ETL	22.30	0.96	83	17.77	81
7	$CH_3NH_3PbI_3$	−3.86	6.21×10^{-3}	ETL	22.10	0.92	84	17.08	81
$PC_{61}BBz$	$CH_3NH_3PbI_3$	−3.80	3.70×10^{-4}	ETL	24.33	0.999	69	16.57	82
$PC_{61}BTh$	$CH_3NH_3PbI_3$	−3.72	3.65×10^{-4}	ETL	24.12	0.950	68	15.74	82
$PC_{61}BPy$	$CH_3NH_3PbI_3$	−3.71	3.66×10^{-4}	ETL	24.85	0.966	74	17.46	82
α-DTC_{70}	$CH_3NH_3PbI_3$	−3.88	3.68×10^{-3}	ETL	22.00	0.874	82.6	15.9	83
β-DTC_{70}	$CH_3NH_3PbI_3$	−3.87	3.51×10^{-3}	ETL	14.09	0.812	76.9	8.80	83
C_{60}-PyP	$CH_3NH_3PbI_3$	−3.89	—	Additive	22.31	1.09	78.26	19.82	27

nucleation Gibbs free energy and controlled crystalline orientation, resulting in improved crystallinity and reduced trap states (Fig. 9c) through the coordination interaction between the N atom of the pyridine and Pb^{2+} ions. As a result, the best PCE reached up to 19.82%, which is dramatically higher than that of the control devices without an additive (17.61%).[27]

All of the above-mentioned Lewis base functionalized fullerene derivatives and their corresponding photovoltaic parameters are summarized in Table 2. Comparing these results, it is found that fullerene derivatives functionalized by amino, oligoether, and crown ether groups are mainly used as CBLs of PSCs sandwiched between ETLs and metal electrodes, which helps to form an interfacial dipole layer for reducing the work function of the metal cathode and promoting the electron transport. The heterocyclic pyridine and thiophene groups bearing the lone pair electrons on N and S atoms respectively can enable the coordination interactions with Pb^{2+} ions of perovskite, leading to an effective passivation of the trap states and promoted charge transport. Therefore, Lewis base functionalized fullerene derivatives are now in the developmental stages and have great potential in boosting the performance of PSCs.

4. Carboxyl and hydroxyl functionalized fullerene derivatives

4.1 Carboxyl functionalized fullerene derivatives

To date, TiO_2 and SnO_2 are two most commonly used ETL materials in planar n–i–p PSCs. However, the oxygen vacancy-related defects at the surface of TiO_2 and SnO_2 ETLs are a notorious charge capture center to deteriorate the electronic properties, leading to poor charge transport as well as serious trap-assistant recombination.[84] To address these issues, in 2013, Snaith and co-workers used a self-assembled monolayer (SAM) of a carboxyl (–COOH)-functionalized fullerene derivative (C_{60}SAM) to modify the mesoporous TiO_2 ETL (Fig. 10). C_{60}SAM acted as an electron acceptor and inhibited electron transfer from the perovskite to TiO_2, resulting in a decrease in energy loss within mesoporous n–i–p PSCs.[85] In a follow-up study, the same group further inserted C_{60}SAM between the perovskite and TiO_2 to construct planar n–i–p $CH_3NH_3PbI_{3-x}Cl_x$ PSCs, achieving the champion PCE of 17.3% with reduced hysteresis (Fig. 11a). C_{60}-SAM incorporation is beneficial for the reduced trap states at the surface and the suppressed nonradiative recombination through the anchoring group of C_{60}-SAM.[86] In 2016, Mora-Sero *et al.* presented three different fullerene derivatives (Fig. 10) functionalized with carboxyl and cyanide groups, which were used as SAMs at the electron selective contact-perovskite interface, leading to a PCE of 13.5% with remarkable reduced *J–V* hysteresis. The grafted carboxyl and cyanide groups within fullerene derivatives could anchor onto the TiO_2 surface and the $CH_3NH_3PbI_{3-x}Cl_x$ perovskite film, respectively, leading to a reduction in capacitive hysteresis observed for oxide-based anodes in PSCs.[87] In the same year, Huang *et al.* used C_{60}SAM and trichloro(3,3,3-trifluoropropyl) silane to construct a hydrophobic cross-linkable fullerene ETL *via* the hydrogen bond interaction between the –COOH of C_{60}SAM and the –OH of the silane coupling molecule as well as the Si–O crosslink bonding. The cross-linkable fullerene ETL could block any accessible pathways of water molecule permeation into $CH_3NH_3PbI_3$ perovskite grain boundaries and protect the underneath perovskite films from moisture-caused erosion (Fig. 11b). Although the cross-linkable fullerene ETL improves the transport properties of the ETL, further doping of a small amount of MAI as an n-type dopant into a fullerene derivative leads to a dramatically increased conductivity of the ETL by over 100-fold. The simultaneous contributions of enhanced conductivity and water-resistance of the ETL led to an improved PCE of 19.5% in the planar p–i–n PSCs and an outstanding moisture stability of the device, retaining more than 90% of its initial PCE after 30 days of storage in air.[88] Likewise, Bo *et al.* applied a simpler carboxyl functionalized fullerene derivative PCBA (Fig. 10) to modify the compact TiO_2 ETL in planar n–i–p PSCs, obtaining a PCE of 17.76% and a V_{oc} of 1.16 V under reverse scanning. PCBA played two important roles in blocking the holes and passivating the trap states on the TiO_2 surface, leading to a reduced charge carrier recombination at the $TiO_2/CH_3NH_3PbI_3$ interface and improving the morphology of the perovskite film.[89]

Multi-adducts of carboxyl functionalized fullerene derivatives were also used in PSCs. In 2015, Gong *et al.* synthesized a novel multi-adduct water/alcohol soluble carboxyl functionalized fullerene derivative ($A_{10}C_{60}$) bearing ten carboxyl groups and incorporated it into the $CH_3NH_3PbI_3$ active layer as an additive to fabricate BHJ-PSCs (Fig. 10). The incorporated $A_{10}C_{60}$ (9.6% w/w) in PSCs helped to balance the carrier extraction efficiency and enlarge the interface between the perovskite and $A_{10}C_{60}$, leading to an improved PCE of 13.97% relative to that of the control device (11.75%).[90] In another study, the same group used $A_{10}C_{60}$ to re-engineer the $PC_{61}BM$ ETL surface to address the poor wettability of PbI_2 atop of the $PC_{61}BM$ layer and to block the hole back transfer into the cathode. As a result, the planar n–i–p $CH_3NH_3PbI_3$ PSCs with $A_{10}C_{60}$ interfacial layers exhibited a PCE of 14.6%.[91]

In 2017, Fang *et al.* synthesized a novel carboxyl functionalized fullerene derivative named as C_{60} pyrrolidine tris-acid (CPTA, Fig. 10) and applied it as an independent ETL to replace the traditional metal oxide ETLs in n–i–p $CH_3NH_3PbI_3$ PSCs, achieving decent PCEs of 18.39% and 17.04% for the glass substrate and the flexible device, respectively. The advantages of the CPTA ETL including outstanding electron mobility, appropriate energy levels, and conformal architecture by covalently anchoring onto the surface of ITO *via* the carboxyl groups are helpful to eliminate photocurrent hysteresis (Fig. 11c) and enhance the long-term stability of devices.[92] In addition, CPTA was also widely used as a modification layer of the traditional metal oxide ETLs in n–i–p PSCs. In 2019, Xu *et al.* utilized CPTA to modify the SnO_2 ETL in flexible n–i–p $CH_3NH_3PbI_3$ PSCs, achieving a PCE of 18.36% and good stability, retaining 87% of its initial PCE after 46 days of exposure to 30% relative humidity at 25 °C without any

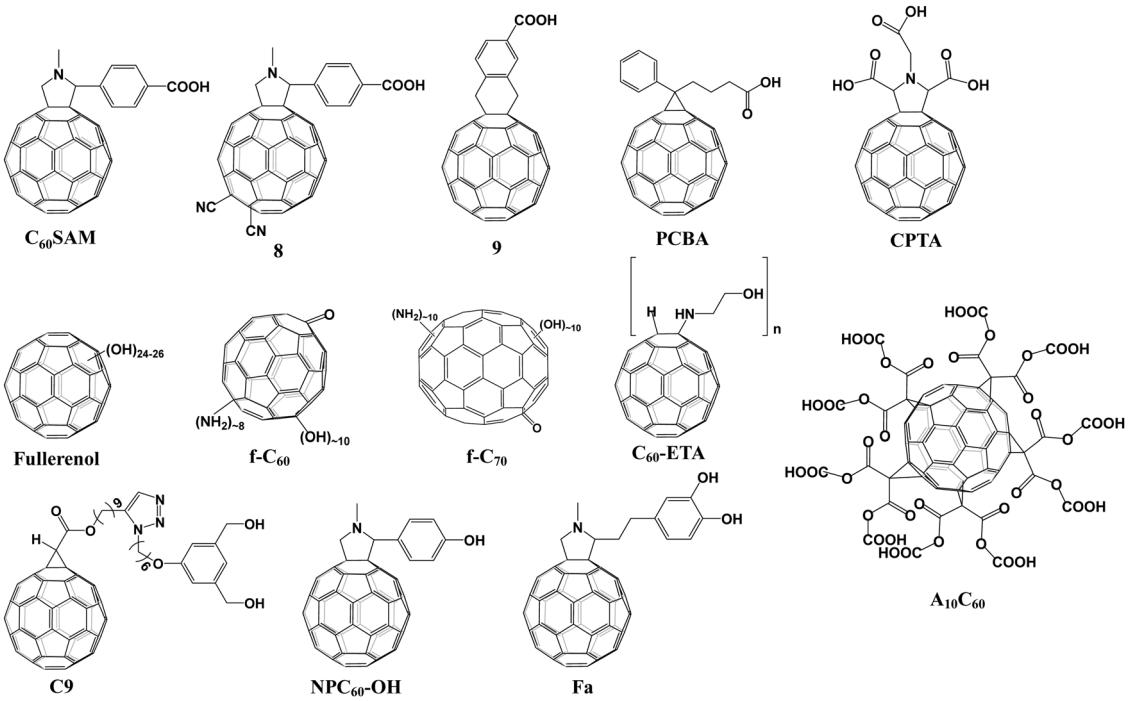

Fig. 10 Molecular structures of carboxyl and hydroxyl functionalized fullerene derivatives applied in PSCs.

encapsulation.[93] In their subsequent study, CPTA was further extended to modify the SnO_2 ETL for constructing planar n–i–p PSCs based on the $FASnI_3$ light-absorbing layer, leading to a PCE of 7.40% and the record V_{oc} of 0.72 V.[94]

Based on these reports, the carboxyl groups grafted onto fullerene have two distinct features, such as the high molecular polarity and the anchoring ability with metal oxide ETLs. Therefore, carboxyl functionalized fullerene derivatives have versatile functions including modifying metal oxide ETLs, additives of perovskite layers, ETLs and interfacial layers in PSCs.

4.2 Hydroxyl functionalized fullerene derivatives

A hydroxyl (–OH) group is another representative polar group possessing the anchoring function with metal oxides similar to the carboxyl group. In 2016, a water-soluble fullerene derivative (fullerenol) with multiple hydroxyl groups (Fig. 10) was first used by Chen *et al.* to modify the TiO_2 ETL in n–i–p PSCs. The fullerenol with excellent conductivity sandwiched between TiO_2 and the $CH_3NH_3PbI_{3-x}Cl_x$ perovskite layer is beneficial for the electron transport and surface wettability of TiO_2, leading to a reduced interfacial resistance and increased crystallinity of the perovskite film. Furthermore, inserting fullerenol into PSCs helps to obtain matched energy level alignments between the perovskite and the cathode. As a result, the PSC devices with fullerenol ETLs deliver the PCE of 14.69%.[95] Later on, the same group further developed two water-soluble fullerene derivatives f-C_{60} and f-C_{70} (Fig. 10) bearing three types of functional groups including –OH, $–NH_2$ and –C═O, and applied them as the buffer layer sandwiched between the C_{60} ETL and the ITO electrode to construct planar n–i–p $CH_3NH_3PbI_{3-x}Cl_x$ PSCs. The PSC devices with a f-C_{60} interlayer afford the champion PCE of 16.97%, which is higher than that of the PSCs with the f-C_{70} interlayer. This is attributed to the higher symmetry of the C_{60} cage than that of f-C_{70}, leading to more even distribution of the functional groups on the fullerene cage and improved energy band alignment.[96] In addition, our group utilized a novel ethanolamine (ETA)-functionalized fullerene derivative C_{60}-ETA (Fig. 10) and $PC_{61}BM$ to successively modify TiO_2 ETLs in planar n–i–p PSCs. The devices based on double fullerene modification layers resulted in an improved PCE of 18.49%, which was higher than that of the single $PC_{61}BM$ or C_{60}-ETA modification layer. This was attributed to the defect passivation of the TiO_2 surface by $PC_{61}BM$, the improved wettability of the $CH_3NH_3PbI_3$ perovskite film on the ETL and more efficient charge transfer between the perovskite and the TiO_2 ETL (Fig. 11d).[97]

In 2018, a hydrophobic fullerene derivative (C9, Fig. 10) bearing long alkyl chains and two hydroxyl groups with anchoring function was used by Zhan *et al.* to modify the SnO_2 ETL in planar n–i–p $(FAPbI_3)_x(MAPbBr_3)_{1-x}$ PSCs, affording a PCE of 21.3%. C9 atop of the SnO_2 ETL efficiently passivated oxygen vacancy-related defects on the SnO_2 surface *via* the covalent bonding of under-coordinated Sn with terminal hydroxyl groups within C9. Moreover, the long and hydrophobic alkyl chain within C9 was beneficial for the ordered molecular self-assembly and forming a non-wetting surface for the perovskite film deposition, leading to the suppressed heterogeneous nucleation and enhanced crystallinity of the perovskite film.[84] In 2019, Chen *et al.* synthesized a pyrrolidinofullerene derivative (NPC_{60}-OH) bearing phenolic hydroxyl (Fig. 10) and applied it to modify the SnO_2 ETL in planar n–i–p PSCs. The reduced energy band gap between the SnO_2 ETL and the perovskite film as well

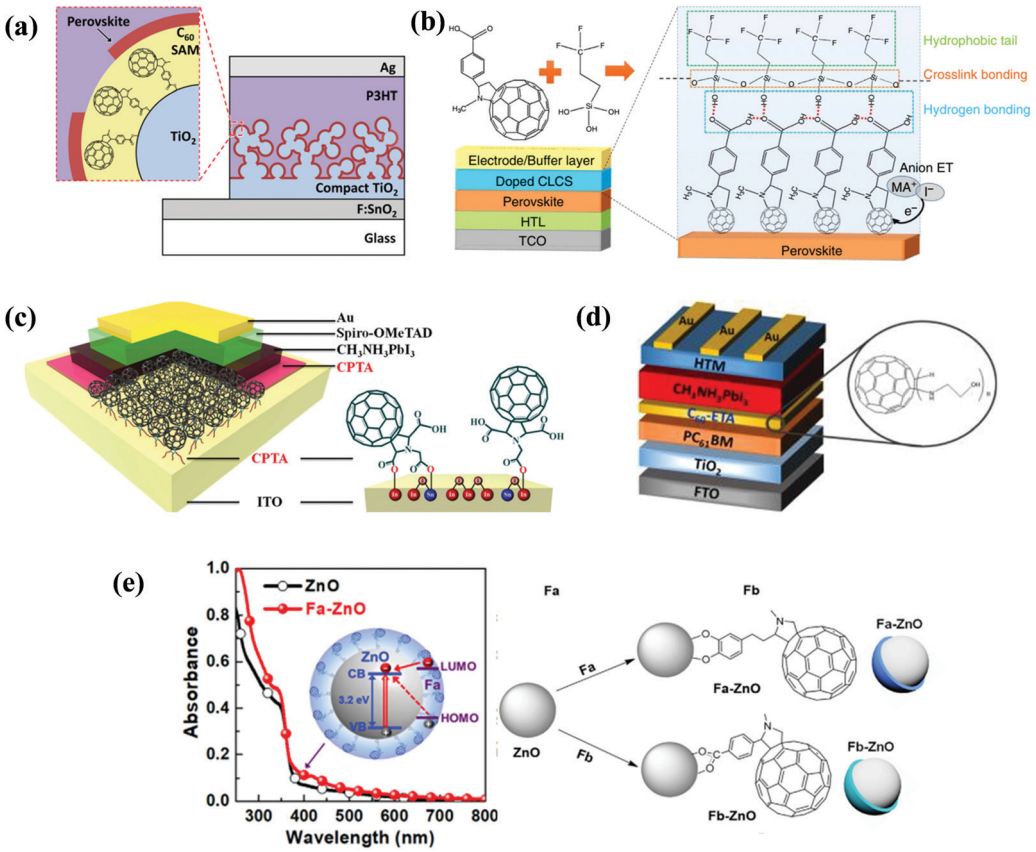

Fig. 11 (a) Schematic of the device structure with C_{60}-SAM atop of the TiO_2 surface. Reproduced with permission from ref. 85. Copyright 2013, American Chemical Society. (b) Device structure of the device and schematic illustration for the crosslinking of C_{60}-SAM with a silane-coupling agent. Reproduced with permission from ref. 88. Copyright 2018, Nature Publishing Group. (c) Schematic illustration of PSC structures with CPTA as the ETL. Reproduced with permission from ref. 92. Copyright 2017, Wiley-VCH. (d) Schematic illustration of PSC structures with C_{60}-ETA. Reproduced with permission from ref. 97. Copyright 2016, Royal Society of Chemistry. (e) UV-visible absorption spectra of the corresponding films and the schematic illustration of fullerene derivatives coated ZnO NPs with core–shell structures. Reproduced with permission from ref. 99. Copyright 2019, Elsevier Inc.

as the increased grain size of the perovskite were realized *via* inserting NPC_{60}-OH to modify the SnO_2 layer, leading to a high PCE of 21.39%.[98]

In 2019, Jen *et al.* reported a catechol-functionalized fullerene derivative (Fa, Fig. 10) which enables strong binding with ZnO *via* covalent bonding between the catechol within Fa and hydroxyl groups on the ZnO nanoparticle surface, resulting in the formation of fullerene-modified ZnO (Fa-ZnO) nanoparticles. On one hand, Fa-ZnO nanoparticles with quasi-core–shell structures facilitate the charge transfer from ZnO nanoparticles to fullerene derivatives *via* the Zn–O–C bonds, leading to the improved electron density in the conduction band of ZnO as well as the reduced work function and enhanced conductivity of Fa-ZnO nanoparticles (Fig. 11e). On the other hand, Fa-ZnO nanoparticles of the n-type heterojunction combined with p-type mesoscopic NiO_x within the perovskite film enable the successful construction of inorganic p–n dual sensitized PSCs. As a result, the devices with $CH_3NH_3PbI_3$ and $FA_{0.85}MA_{0.15}PbI_{2.55}Br_{0.45}$ light-absorbing layers afford PCE as high as 20.2% and 21.1%, respectively. Furthermore, the high-quality Fa-ZnO nanoparticle ETL greatly enhances the device long-term stability due to the reduced trap states, the inhibited ion migration and moisture diffusion.[99]

In order to compare the performance of different fullerene derivatives, the above-mentioned carboxyl and hydroxyl functionalized fullerene derivatives and their corresponding photovoltaic parameters are summarized in Table 3. The polar carboxyl and hydroxyl groups are able to anchor metal oxide ETLs to passivate the oxygen vacancy-related defects on the surface of metal oxide ETLs. The modification of metal oxide ETLs by these polar fullerene derivatives helps to achieve higher electron transport, suitable energy level alignments and reduced charge carrier recombination. Furthermore, the increased surface wettability after inserting these polar fullerene derivatives is beneficial for forming a continuous and compact perovskite film and suppressing the heterogeneous nucleation, affording a high-quality perovskite film with large grain size and optimized grain orientation for remarkably decreased trap states and increased charge carrier mobility. Besides, these polar fullerene derivatives have another role in acting as independent ETLs or double ETLs, in which fullerene derivatives enable the strong chemical interaction with ITO or FTO for matched energy level alignment and trap state passivation. Based on the advantages of these carboxyl or hydroxyl functionalized fullerene derivatives, modulating these

Table 3 Device performance of PSCs based on carboxyl and hydroxyl functionalized fullerene derivatives

Compound	Active layer	LUMO (eV)	μ ($cm^2\ V^{-1}\ s^{-1}$)	Role of the molecule	J_{sc} (mA cm^{-2})	V_{oc} (V)	FF (%)	PCE (%)	Ref.
C_{60}SAM	$CH_3NH_3PbI_{3-x}Cl_x$	−3.95	—	Modifying TiO_2	22.1	1.04	0.75	17.3	86
8	$CH_3NH_3PbI_{3-x}Cl_x$	−4.20	—	Modifying TiO_2	19.40	0.79	76	10.8	87
9	$CH_3NH_3PbI_{3-x}Cl_x$	−4.00	—	Modifying TiO_2	19.8	0.85	71	11.7	87
PCBA	$CH_3NH_3PbI_3$	−4.2	—	Modifying TiO_2	21.38	1.16	72	17.76	89
CPTA	$CH_3NH_3PbI_3$	−3.9	5.4×10^{-3}	ETL	22.06	1.10	75.61	18.39	92
CPTA	{en}$FASnI_3$	−3.9	—	Modifying SnO_2	16.45	0.687	65	7.40	94
$A_{10}C_{60}$	$CH_3NH_3PbI_3$	−4.1	—	Additive	19.41	0.88	81.6	13.97	90
WS-C_{60}	$CH_3NH_3PbI_3$	−4.1	—	Modifying $PC_{61}BM$	27.4	0.95	56	14.6	91
Fullerenol	$CH_3NH_3PbI_{3-x}Cl_x$	−4.27	—	Modifying TiO_2	21.28	0.96	72	14.7	95
f-C_{60}	$CH_3NH_3PbI_{3-x}Cl_x$	−4.45	—	ETL	21.32	1.04	76.25	16.97	96
f-C_{70}	$CH_3NH_3PbI_{3-x}Cl_x$	−4.42	—	ETL	21.21	1.03	72.58	15.94	96
C_{60}-ETA	$CH_3NH_3PbI_3$	−3.72	—	ETL	23.76	1.06	69	18.49	96
C9	$(FAPbI_3)_x(MAPbBr_3)_{1-x}$	−4.03	—	Modifying SnO_2	24.1	1.12	78.9	21.3	84
NPC_{60}-OH	Perovskite	−4.14	—	Modifying SnO_2	23.37	1.13	80.73	21.39	98
Fa	$FA_{0.85}MA_{0.15}PbI_{2.55}Br_{0.45}$	—	—	Modifying ZnO	22.83	1.14	81	21.11	99

functional groups including the number and steric locations should be further investigated so as to improve their performance in PSCs.

5. Halogen functionalized fullerene derivatives

Interestingly, simple halogen atoms such as Cl, Br and F have been demonstrated to be magic elements in PSCs after being grafted onto the fullerene cage. Incorporating the halogen-functionalized fullerene derivatives into PSCs has been revealed to enlarge the grain size, reduce current-voltaic hysteresis, and increase the charge recombination resistance as well as the stability of the device.[100–105] In 2018, Wang *et al.* synthesized three fulleropyrrolidine derivatives with different substituents (H, Cl and Br) abbreviated as NAMF-H, NAMF-Cl and NAMF-Br (Fig. 12) to study the influence of halogen atoms within fullerene derivatives on the performance of planar n–i–p $CH_3NH_3PbI_3$ PSCs. Their results showed that NAMF-Cl applied as the interfacial layer atop the TiO_2 ETL in PSCs afforded the best PCE of 19.3%, which was attributed to the better co-planarity of the functional group and higher electron mobility. Furthermore, the chlorine atom in NAMF-Cl was unveiled to interact with the TiO_2 ETL with the formation of a O═Ti–Cl bond, benefiting the defect passivation and the enlarged grain size.[100]

In particular, compounds containing fluorine atoms were usually evidenced to possess strong hydrophobicity and low surface energy which helps to improve the ambient stability of perovskites.[101] Therefore, introducing fluorinated groups into fullerene derivatives to form novel fluoro-functionalized fullerene derivatives is highly desirable. In 2016, Jen *et al.* reported a fluoroalkyl substituted hydrophilic fullerene (DF-C_{60}, Fig. 12) which was applied as an additive of the $CH_3NH_3PbI_3$ perovskite to construct fullerene/perovskite p–i–n BHJ-PSCs, yielding a PCE of 18.11% with increased stability and reduced trap-states. The incorporated DF-C_{60} with low surface energy mainly located at the upper surface and grain boundaries of the perovskite film, helping to reduce the current–voltage hysteresis and passivate the defects as well as enhance the ambient stability.[102] One year later, the same group adopted an anti-solvent approach to

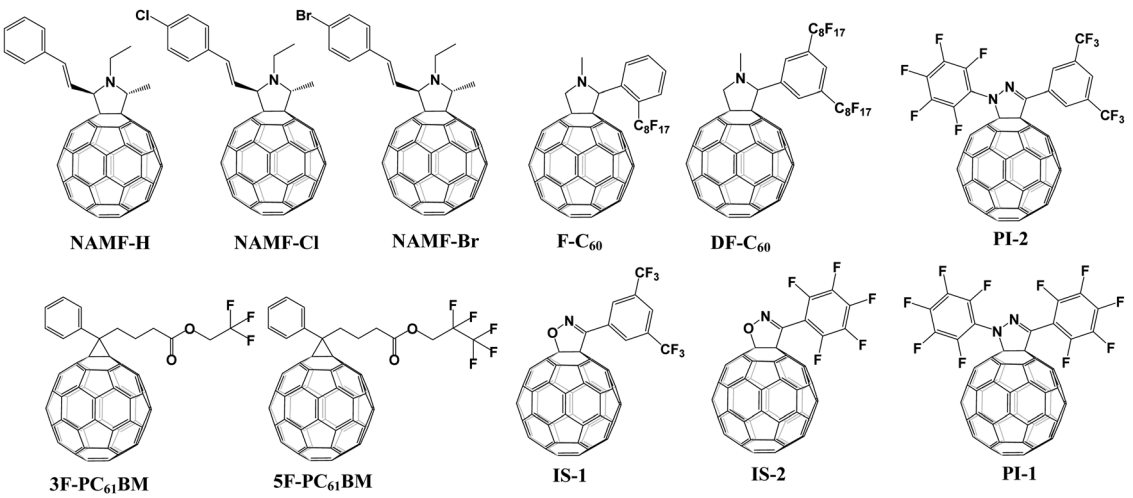

Fig. 12 Molecular structures of halogen functionalized fullerene derivatives applied in PSCs.

incorporate DF-C_{60} into the low-bandgap Pb–Sn binary perovskite ($CH_3NH_3Pb_{0.5}Sn_{0.5}I_3$) for the preparation of graded heterojunction PSCs. A graded distribution of DF-C_{60} in the perovskite film effectively passivated defects, decreased the number of trap sites and improved the absorber quality, leading to an improved PCE of 15.61% and a high V_{oc} (0.89 V).[103] Likewise, they also synthesized another novel fluoroalkyl substituted fullerene derivative (F-C_{60}) with only one C_8F_{17} group (Fig. 12), and combined it with bis-C_{60} to form a hybrid fullerene cathode interlayer in p–i–n PSCs. The hybrid fullerene cathode interlayer simultaneously possesses the advantage of F-C_{60} and bis-C_{60}, including the appealing electrical conductivity and lower surface energy which are beneficial for enhanced charge collection from the $CH_3NH_3PbI_{3-x}Cl_x$ perovskite to the electrode and suppressed charge recombination in the perovskite light-absorbing layer. As a result, devices with a PCE of 15.5% and excellent stability retaining nearly 80% of their initial PCE after being exposed under ambient conditions (20% RH) for two weeks without any encapsulation were achieved.[104] In 2018, Su *et al.* synthesized two fluorinated $PC_{61}BM$ derivatives (3F-$PC_{61}BM$ and 5F-$PC_{61}BM$, Fig. 12) and incorporated them as additives into the perovskite light-absorbing layer to study the effect of fluoroalkyl chain length within fullerene derivatives on the $CH_3NH_3PbI_3$ perovskite film quality and device performance. Incorporating 0.1 wt% of the 3F-$PC_{61}BM$ additive into the perovskite film enabled the formation of BHJ perovskite and densely packed perovskite grains, which helped to passivate the defects within the perovskite and suppress the permeation of moisture into the grain boundaries under ambient conditions. As a result, the devices with 3F-$PC_{61}BM$ additives afforded a PCE of 16.17%, which was much higher than that of the device based on 5F-$PC_{61}BM$ (8.65%). Besides, the device stability was improved after incorporating 3F-$PC_{61}BM$, maintaining 80% of the initial efficiency after 550 hours of storage under ambient conditions (25 °C, 50% relative humidity). The results unveiled that 5F-$PC_{61}BM$ with a longer fluoroalkyl chain is prone to undergo self-aggregation more easily than that of 3F-$PC_{61}BM$ in the perovskite film, leading to a large amount of heterogeneous nucleation sites, which is responsible for the discontinuous rough film morphology with more voids.[105] In addition to the above fluoroalkyl chain substituted fullerene derivatives, the fluorine substituted phenyls were also used to functionalize fullerene, affording a variety of novel fluoro-functionalized fullerene derivatives (IS-1, IS-2, PI-1 and PI-2, Fig. 12), which were applied to construct ETL-free PSCs based on perovskite:fullerene hybrid films. The as-prepared n–i–p PSCs based on the $CH_3NH_3PbI_3$:IS-2 blend film exhibit the highest PCE of 14.3%.[106]

All of these halogen functionalized fullerene derivatives and their corresponding photovoltaic parameters are summarized in Table 4. We can conclude that grafting halogen atoms onto the fullerene cage generates some unique properties, rendering superior performance of the corresponding fullerene derivatives upon being applied as additives or modification layers in PSCs. Chlorine functionalized fullerene derivatives have the features of regulating the coplanarity of the pendent groups and interacting with TiO_2 to passivate defects. As for the fluorine functionalized fullerene derivatives, the introduced fluorine atoms are beneficial for improving the solubility of fullerene derivatives in polar solvents such as DMF for a facile fabrication procedure. On the other hand, fluorine substituted fullerene derivatives have low surface energy, helping to fabricate the grade heterojunction perovskite light-absorbing layer and to suppress the penetration of moisture into the grain boundaries of the perovskite for efficient and stable PSCs. Therefore, in order to address the inferior stability of PSCs based on organic lead halide perovskites, developing novel fluorine substituted hydrophobic fullerene derivatives appears to be an effective strategy to passivate the grain boundaries and improve the ambient stability simultaneously.

6. Cross-linked fullerene derivatives

6.1 Thermal cross-linked fullerene derivatives

In 2016, Snaith *et al.* applied two cross-linked fullerene derivatives (sol–gel C_{60} and PCBCB, Fig. 13) as n-type charge collection layers in planar n–i–p $CH_3NH_3PbI_{3-x}Cl_x$ PSCs, leading to a PCE of 17.9% for both cross-linked fullerene ETLs. Cross-linked sol–gel C_{60} *via* hydrolysis-condensation reactions and cross-linked PCBCB *via* annealing at 200 °C (Fig. 14a) could generate two types of insoluble fullerene films which are beneficial for the electron-selective contacts and reduced shunting paths toward improved hole-blocking and excellent charge transport ability.[107] In 2016, Liao *et al.* synthesized another thermal cross-linked fullerene derivative (C-PCBSD, Fig. 13) and

Table 4 Device performance of PSCs based on halogen functionalized fullerene derivatives

Compound	Active layer	LUMO (eV)	μ ($cm^2\ V^{-1}\ s^{-1}$)	Role of the molecule	J_{sc} (mA cm^{-2})	V_{oc} (V)	FF (%)	PCE (%)	Ref.
NAMF-H	$CH_3NH_3PbI_3$	−4.05	3.7×10^{-4}	Modifying TiO_2	22.4	1.08	78.4	19.0	100
NAMF-Cl	$CH_3NH_3PbI_3$	−4.08	1.44×10^{-3}	Modifying TiO_2	22.7	1.08	78.6	19.3	100
NAMF-Br	$CH_3NH_3PbI_3$	−4.13	3.6×10^{-4}	Modifying TiO_2	21.8	1.10	79.7	19.1	100
DF-C_{60}	$CH_3NH_3PbI_3$	—	1.8×10^{-3}	Additive	21.08	1.09	78.7	18.11	102
DF-C_{60}	$CH_3NH_3Pb_{0.5}Sn_{0.5}I_3$	—	—	Additive	26.1	0.87	69	15.61	103
F-C_{60}	$CH_3NH_3PbI_{3-x}Cl_x$		3.2×10^{-4}	CBL	21.2	0.97	75.4	15.5	104
3F-$PC_{61}BM$	$CH_3NH_3PbI_3$	−4.2	5.61×10^{-4}	Additive	21.78	1.00	73.34	16.17	105
5F-$PC_{61}BM$	$CH_3NH_3PbI_3$	−4.2	2.69×10^{-4}	Additive	14.99	0.87	65.71	8.65	105
IS-1	$CH_3NH_3PbI_3$	−4.06	—	Additive	16.7	1.03	69	11.8	106
IS-2	$CH_3NH_3PbI_3$	−4.05	—	Additive	16.1	1.06	73.8	12.7	106
IP-1	$CH_3NH_3PbI_3$	−4.08	—	Additive	—	—	—	—	106
IP-2	$CH_3NH_3PbI_3$	−4.08	—	Additive	16.1	1.02	69.4	11.7	106

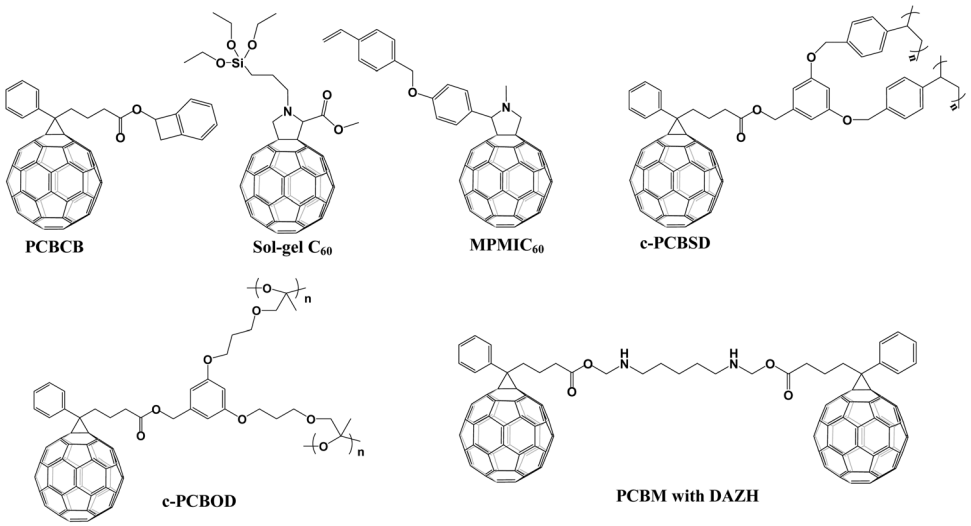

Fig. 13 Molecular structures of cross-linked fullerene derivatives applied in PSCs.

introduced it into the $CH_3NH_3PbI_xCl_{3-x}$ perovskite to enhance the crystallization of the perovskite film and electron extraction efficiency *via* an anti-solvent method. A cross-linked network of C-PCBSD could protect the perovskite layer from the erosion of moisture and passivate the defects in the bulk perovskite films, affording a PCE of 17.21%.[108] Later on, the same group prepared a face-on stacked composite film composed of a large π-conjugated graphdiyne (GD) and C-PCBSD *via* π–π stacking interaction, which exhibited superior features including high electron mobility, efficient charge extraction and energy-level tailoring. Moreover, the ordered orientation of the C-PCBSD/GD composite film (Fig. 14b) not only benefited the growth of the high-quality $CH_3NH_3PbI_3$ perovskite film, but also provided sufficient solvent resistance to avoid the interfacial erosion during the process of depositing the perovskite precursor. Consequently, the PSC devices with C-PCBSD/GD composite films offered an improved PCE up to 20.19% and enhanced device stability.[109] In 2017, Petrozza *et al.* also applied C-PCBSD as an electron extraction layer atop the TiO_2 ETL in planar n–i–p PSCs. *In situ* cross-linked C-PCBSD is vital for the interface

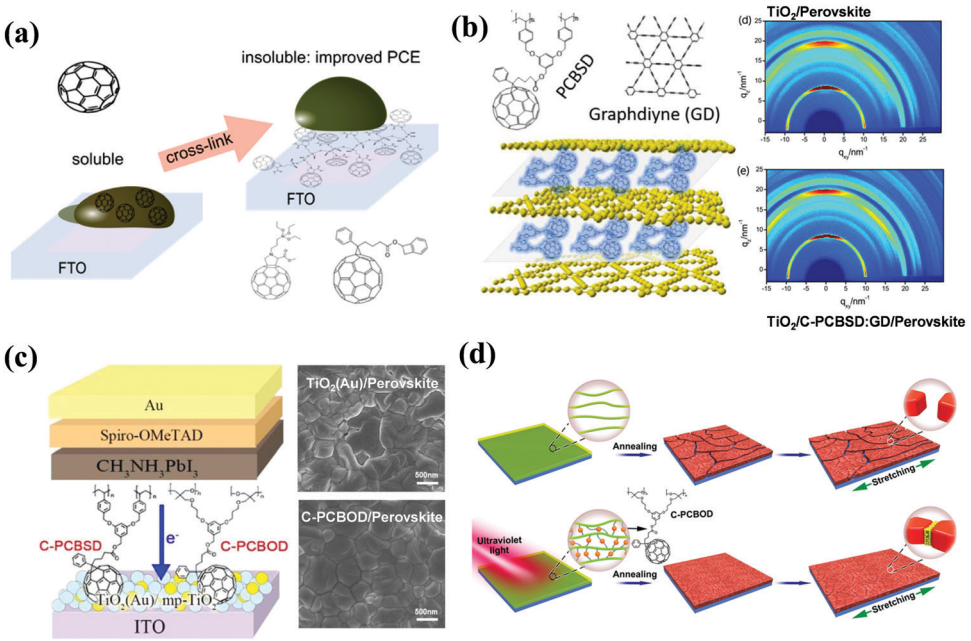

Fig. 14 (a) Schematic illustration of cross-linked processes. Reproduced with permission from ref. 107. Copyright 2016, American Chemical Society. (b) Schematic illustration for the face on stacked C-PCBSD film owing to the π–π stacking interaction and the corresponding 2D GIXRD patterns. Reproduced with permission from ref. 109. Copyright 2017, Elsevier Ltd. (c) Schematic illustration of the device configuration and scanning electron microscopy (SEM) top-view images of the corresponding perovskite films. Reproduced with permission from ref. 112. Copyright 2017, American Chemical Society. (d) Operational mechanism of C-PCBOD. Reproduced with permission from ref. 113. Copyright 2019, Wiley-VCH.

energetics and the electronic quality of the $CH_3NH_3PbI_3$ perovskite layer, which contribute to the minimized carrier recombination losses. As a result, the device with a C-PCBSD electron extraction layer exhibited an obviously enhanced PCE close to 19% with a V_{oc} larger than 1.1 V.[110]

In addition to C-PCBSD, another thermal cross-linked styrene-functionalized fullerene derivative $MPMIC_{60}$ (Fig. 13) was synthesized to replace the traditional $PC_{61}BM$ and C_{60} ETL in both regular and inverted PSCs. After annealing at 250 °C, $MPMIC_{60}$ could cross-link to form an insoluble solvent-resistant film with improved fracture resistance, leading to higher V_{oc} and J_{sc} values in planar n–i–p $CH_3NH_3PbI_3$ PSCs.[111]

6.2 Photo cross-linked fullerene derivatives

In addition to thermal cross-linking with styrene groups as active sites, epoxy is another commonly used group which can undergo light-crosslinking under mild conditions. In 2017, Hsu *et al.* prepared a novel fullerene derivative (C-PCBOD, Fig. 13) and applied it as a cross-linkable material to modify the surface of the TiO_2 ETL in n–i–p PSCs. The cross-linked PCBOD film formed *via* UV-curing provided a superior surface coverage toward the TiO_2 ETL and a water-resistant layer to protect it from solvent erosion in the process of depositing the $CH_3NH_3PbI_3$ perovskite film. Cross-linked PCBOD between the TiO_2 ETL and the perovskite layer passivated the trap-states of TiO_2, which was favorable for the excellent electron extraction and the retarded charge recombination (Fig. 14c), delivering an improved PCE of 15.9% and 18.3% for the compact TiO_2 and mesoporous-TiO_2 ETL, respectively.[112]

In 2019, Liao *et al.* introduced a photo-crosslinked fullerene derivative (C-PCBOD) as a plasticizer (Fig. 14d) into the perovskite film, which distributes around the perovskite grain boundaries, leading to improved mechanical and moisture stability of the perovskite film. Furthermore, embracing the perovskite grain boundaries *via* C-PCBOD was able to passivate the defects and block the degradation of devices by suppressing the penetration of moisture along the perovskite grain boundaries. As a result, the $CH_3NH_3PbI_3$ PSCs with C-PCBOD achieve a high PCE of 20.4% and 18.1% for rigid and flexible substrates, respectively.[113]

In 2017, a new cross-linked approach was reported by Cheyns *et al.*, in which 1,6-diazidohexane (DAZH, Fig. 13) as a bridge tether was utilized to cross-link the neighboring $PC_{61}BM$ for the preparation of cross-linked $PC_{61}BM$ through the highly reactive nitrenes and C–H insertion. In addition to the outstanding electron extraction capability, the cross-linked $PC_{61}BM$ as the interlayer atop the TiO_2 ETL shows excellent solvent-resistant ability for suppressing the wash away of the perovskite precursor toward the $PC_{61}BM$ interlayer in the process of spin-coating the perovskite film. The $(HC(NH_2)_2)_{0.66}(CH_3NH_3)_{0.34}PbI_{2.85}Br_{0.15}$ PSCs with cross-linked interlayers afford a PCE of 18.4% and 14.9% for small-area devices and 4 cm^2 perovskite solar modules, respectively.[114]

Table 5 summarizes all reported cross-linked fullerene derivatives applied in PSCs and their corresponding photovoltaic parameters. Cross-linked fullerene derivatives have two merits including strong electron extraction capability and superior solvent-resistance, beneficial for improving the electron extraction from the perovskite film to the ITO electrode and enhancing the stability of the PSC device. It is well known that fullerene derivatives with superior electron extraction and transport ability have been widely applied as ETLs in planar p–i–n PSCs. However, the wash away of fullerene derivative ETLs from *N*,*N*-dimethylformamide (DMF) or dimethyl sulfoxide (DMSO) during the spin-coating process of the perovskite film is a critical issue to restrict the application of fullerene derivatives in planar n–i–p PSCs. Cross-linked fullerene derivatives provide an effective approach to address this issue. The incorporation of cross-linked fullerene derivatives into n–i–p PSCs is beneficial for improving the electron extraction from the perovskite film to the ITO electrode and enhancing the device stability. The as-formed organic networks of cross-linked fullerene derivatives can further improve mechanical stability and charge transfer of the device, resulting in enhanced device performance. However, the reported cross-linked fellerene derivatives applied in PSCs are still limited to styryl and epoxy. Therefore, developing new cross-linked fullerene derivatives bearing other cross-linkable groups is highly desirable toward improved device stability and flexible devices.

7. Other fullerene derivatives

Except for the abovementioned fullerene derivatives which can be classified clearly according to the functional groups, a number of other fullerene derivatives including ICBA and ICBA-like fullerene derivatives, fulleropyrrolidine derivatives and dimeric fullerene derivatives have been also applied in PSCs, which are described as follows, and their chemical

Table 5 Device performance of PSCs incorporating cross-linked fullerene derivatives

Compound	Active layer	LUMO (eV)	μ ($cm^2\ V^{-1}\ s^{-1}$)	Role of the molecule	J_{sc} (mA cm^{-2})	V_{oc} (V)	FF (%)	PCE (%)	Ref.
Sol–gel C_{60}	$CH_3NH_3PbI_{3-x}Cl_x$	—	3.8×10^{-4}	ETL	23.0	1.07	73	17.9	107
PCBCB	$CH_3NH_3PbI_{3-x}Cl_x$	—	5.9×10^{-3}	ETL	22.4	1.11	73	17.9	107
C-PCBSD	$CH_3NH_3PbI_3$	—	—	Modifying TiO_2	21.1	1.12	79.0	18.7	110
C-PCBSD	$CH_3NH_3PbI_{3-x}Cl_x$	—	—	Additive	22.81	0.98	77	17.21	108
$MPMIC_{60}$	$CH_3NH_3PbI_3$	−4.1	—	ETL	20.2	1.08	64	13.8	111
C-PCBOD	$CH_3NH_3PbI_3$	−3.8	—	Modifying TiO_2	23.99	1.041	73.25	18.29	112
C-PCBOD	$CH_3NH_3PbI_3$	—	—	Additive	22.60	1.14	79	20.4	113
$PC_{61}BM$ with DAZH	$CH_3NH_3PbI_3$	—	—	ETL	20.3	1.08	77.9	17.1	114

Table 6 Device performance of PSCs incorporating some functionalized fullerene derivatives

Compound	Active layer	LUMO (eV)	μ ($cm^2\ V^{-1}\ s^{-1}$)	Role of the molecule	J_{sc} ($mA\ cm^{-2}$)	V_{oc} (V)	FF (%)	PCE (%)	Ref.
ICBA	$CH_3NH_3PbI_3$	−3.6	6.9×10^{-3}	ETL	10.03	0.58	58	3.4	33
ICTA	$CH_3NH_3PbI_3$	—	—	ETL	22.1	1.10	74.2	18.04	118
IPB	$CH_3NH_3PbI_3$	−3.94	—	ETL	16.28	1.102	78	14.02	46
IPH	$CH_3NH_3PbI_3$	−3.94	—	ETL	16.70	1.107	79	14.64	46
$C_{60}(CH_2)$(Ind)	$CH_3NH_3PbI_3$	−3.66	3.0×10^{-3}	ETL	20.4	1.13	80	18.1	119
C5-NCMA	$CH_3NH_3PbI_3$	−3.87	1.59×10^{-3}	ETL	20.68	1.08	79.1	17.6	120
EDNC	$CH_3NH_3PbI_3$	−3.86	8.5×10^{-5}	ETL	19.85	0.95	66.92	12.64	121
BDNC	$CH_3NH_3PbI_3$	−3.86	7.7×10^{-5}	ETL	16.17	0.93	48.72	7.36	121
IBF-Ep	$CH_3NH_3PbI_{3-x}Cl_x$	−4.40	—	ETL	16.9	0.86	62	9.0	122
C_{60}(9MA)	$CH_3NH_3PbI_3$	—	—	ETL	21.1	0.984	72.3	15.0	123
ICMA	$CH_3NH_3PbI_3$	−3.85	—	ETL	20.0	1.07	64.7	13.9	124
$DMEC_{60}$	$CH_3NH_3PbI_3$	−3.89	7.21×10^{-4}	ETL	21.73	0.92	75.8	15.2	125
$DMEC_{70}$	$CH_3NH_3PbI_3$	−3.90	9.07×10^{-4}	ETL	22.44	0.95	77.1	16.4	125
$C_{60}MC_{12}$	$CH_3NH_3PbI_{3-x}Br_x$	−4.16	—	ETL	17.45	1.24	77	16.74	47
Bis-$DMEC_{60}$	$(5\text{-AVA})_{0.03}(MA)_{0.97}PbI_3$	−3.80	—	Modifying TiO_2	23.30	0.92	71	15.21	126
DPC_{60}	$Cs_{0.05}(MA_{0.17}FA_{0.83})_{0.95}Pb(I_{0.83}Br_{0.17})_3$	−3.9	1.03×10^{-3}	Modifying SnO_2	23.0	1.14	77.7	20.4	127
CPTA-E	$CH_3NH_3PbI_3$	−4.18	3.8×10^{-4}	ETL	20.22	1.103	78.22	17.44	128
PDI-C_{60}	$CH_3NH_3PbI_3$	−3.96	8.76×10^{-4}	ETL	22.1	1.061	79.2	18.6	129
D-C_{60}	$CH_3NH_3PbI_3$	−3.88	9.83×10^{-4}	ETL	21.89	0.96	78.8	16.6	131
d-$PC_{61}BM$	$CH_3NH_3PbI_{3-x}Cl_x$	—	—	ETL	16.70	0.941	73	11.43	130

structures along with the corresponding photovoltaic parameters are summarized in Table 6.

7.1 ICBA and ICBA-like fullerene derivatives

In 2013, Chen *et al.* first applied the indene-C_{60} bisadduct ($IC_{60}BA$, Fig. 15) as an ETL of planar p–i–n $CH_3NH_3PbI_3$ PSCs, which afforded a low PCE of 3.4%.[33] In 2015, Jen *et al.* also used $IC_{60}BA$ as the ETL in planar p–i–n $CH_3NH_3PbI_3$ PSCs in which the $IC_{60}BA$ ETL was modified by the bis-C_{60} layer, achieving a PCE of 8.06%.[115] In 2016, Chang *et al.* deposited the $IC_{60}BA$ ETL atop the $CH_3NH_3PbBr_3$ light-absorbing layer to form a pseudo BHJ structure by the penetration of $IC_{60}BA$ into the defects/voids of the $CH_3NH_3PbBr_3$ film. The devices combining the $IC_{60}BA$ ETL and solvent annealing procedure afforded a PCE of 7.50% and a high V_{oc} of 1.60 V.[116] In 2017, Huang *et al.* applied the isomeric pure $IC_{60}BA$-tran3 as the ETL to construct wide-bandgap $(FA_{0.83}MA_{0.17})_{0.95}Cs_{0.05}Pb(I_{0.6}Br_{0.4})_3$ PSCs, accomplishing a high PCE of 18.5% with a high V_{oc} of 1.21 V. The superiority of $IC_{60}BA$-tran3 relative to the $IC_{60}BA$-mixture is due to the reduced energy disorder and the increased conductivity, consequently improving the device efficiency of PSCs.[117] Moreover, Neher *et al.* pointed out that the indene-C_{60}-trisadduct (ICTA, Fig. 15) with the lowest electron affinity applied as an ETL of planar p–i–n $CH_3NH_3PbI_3$ PSCs is responsible for the highest V_{oc} among C_{60}, $PC_{61}BM$ and ICTA ETLs. The higher LUMO energy level of ICTA than those of $PC_{61}BM$ and C_{60} ETLs leads to an efficient reduction of V_{oc} losses due to the proper energy alignment, exhibiting an improved PCE of 18.04% and a V_{oc} of 1.1 V.[118]

In addition to $IC_{60}BA$, a series of $IC_{60}BA$-like fullerene derivatives were developed to act as ETLs in PSCs. In 2016, Bolink *et al.* unveiled that two $IC_{60}BA$-like fullerene derivatives (IPB, IPH, Fig. 15) bearing, respectively, butyl and hexyl ester can form high quality ETLs with fewer defects in p–i–n $CH_3NH_3PbI_3$ PSCs, resulting in enhanced J_{sc} and V_{oc}. The device with IPB and IPH ETLs exhibited improved PCEs of 14.02% and 14.64%, respectively.[46] Later on, Cao *et al.* synthesized a $IC_{60}BA$-like fullerene derivative $C_{60}(CH_2)$(Ind) (Fig. 15). The incorporation of $C_{60}(CH_2)$(Ind) as the ETL in p–i–n $CH_3NH_3PbI_3$ PSCs enables more efficient interfacial defect passivation, improved electron extraction and suppressed trap-assisted recombination (Fig. 16a), leading to an outstanding PCE of 18.1% and V_{oc} of 1.13 V which are higher than those of the $PC_{61}BM$-based device (16.2% and 1.05 V). The improved V_{oc} is obtained from the higher LUMO energy levels (−3.66 V) of $C_{60}(CH_2)$(Ind) than that of $PC_{61}BM$ (−3.8 eV).[119] Another $IC_{60}BA$-like fullerene derivative (C5-NCMA, Fig. 15) with two pentyloxy chains was synthesized by Yang *et al.* and used as the ETL to replace the $PC_{61}BM$ ETL in planar inverted PSCs. Due to the higher LUMO energy level and more efficient electron extraction/electron transport of the C5-NCMA ETL than that of $PC_{61}BM$, the $CH_3NH_3PbI_3$ PSC devices delivered an improved PCE of 17.6% with negligible hysteresis.[120] Similarly, Xie *et al.* prepared two fullerene derivatives (EDNC and EBNC, Fig. 15) in 2017, which have similar structures to that of C5-NCMA except for the number of pendent chains, and applied it as the ETL in p–i–n $CH_3NH_3PbI_3$ PSCs. The devices with EDNC and EBNC ETLs achieved PCEs of 12.64% and 7.36%, respectively, which are however lower than that of the device with the $PC_{61}BM$ ETL (15.04%). The inferior performance of EDNC and EBNC relative to that of C5-NCMA indicates that the minor tailoring of the functional groups within such fullerene derivatives can lead to a distinct performance difference.[121]

Gradečak *et al.* used the Diels–Alder reaction to synthesize a new fullerene derivative isobenzofulvene-C_{60}-epoxide (IBF-Ep, Fig. 15) and used it as the ETL to replace the $PC_{61}BM$ ETL in both n–i–p and p–i–n $CH_3NH_3PbI_{3-x}Cl_x$ PSCs. Due to the bulky epoxidized isobenzofulvene appendage which is beneficial for suppressing solid state phase transitions, the IBF-Ep ETL exhibits excellent morphological stability under thermal stress and good compatibility with the $CH_3NH_3PbI_{3-x}Cl_x$ perovskite, leading to a PCE of 9.0% for p–i–n PSCs.[122] Another soluble

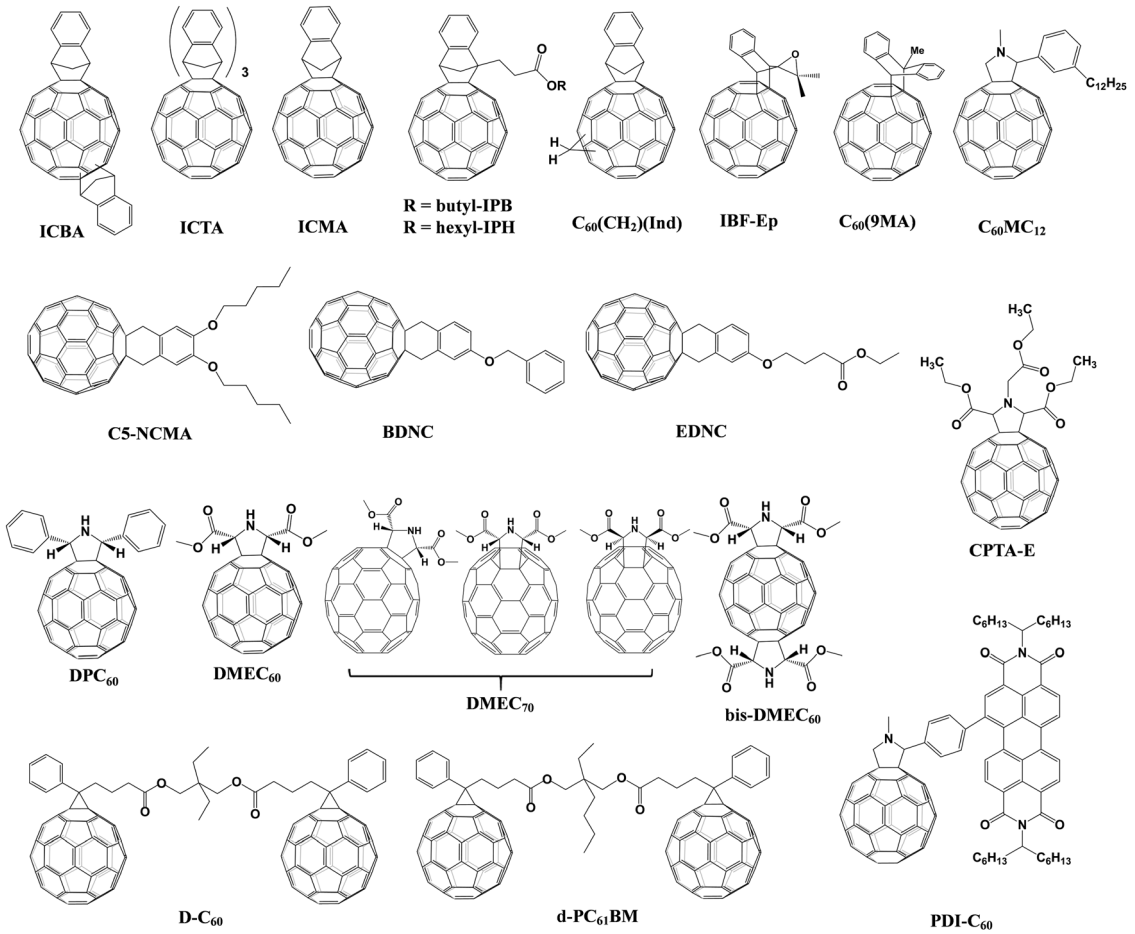

Fig. 15 Molecular structures of other functionalized fullerene derivatives applied in PSCs.

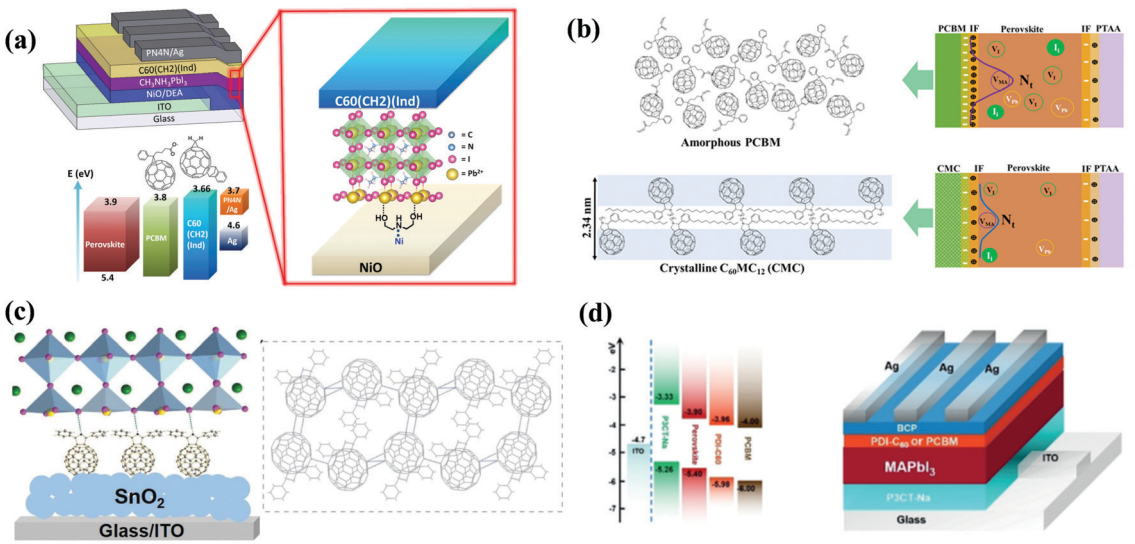

Fig. 16 (a) Schematic illustration of PSC structures and energy-level. Reproduced with permission from ref. 119. Copyright 2017, Wiley-VCH. (b) Schematic illustration of the mechanism involving crystalline fullerene derivatives for enhancement in device performances. Reproduced with permission from ref. 47. Copyright 2018, American Chemical Society. (c) Schematic illustration of interfacial modification and the corresponding molecular packing. Reproduced with permission from ref. 127. Copyright 2019, Wiley-VCH. (d) Corresponding energy-level diagram and device structures of PSCs. Reproduced with permission from ref. 129. Copyright 2019, Wiley-VCH.

fullerene derivative C_{60}-9-methylanthracene mono-adduct (C_{60}(9MA), Fig. 15) synthesized *via* the Diels–Alder reaction was developed by Imahori *et al.* and was used as a thermal precursor to the C_{60} electron selective layer (ESL) in planar n–i–p $CH_3NH_3PbI_3$ PSCs. The superior film-forming property by using the thermal precursor approach afforded a remarkably improved FF (72.3%) and a PCE (15.0%) of the device relative to that of the TiO_2-based device (FF of 67.1% and PCE of 12.9%).[123] In 2017, Albrecht *et al.* systematically studied the influence of fullerene derivative (C_{60}, $PC_{61}BM$, ICMA) ETLs on the device performance of n–i–p PSCs. They found that the devices with independent ICMA ETLs (Fig. 15) exhibited an averaged PCE of 13.9%, while those based on TiO_2/$PC_{61}BM$ double-layer ETLs afforded a stabilized PCE of 18.0% and negligible photocurrent hysteresis. The undesirable PCE of the ICMA ETL is perhaps attributed to the lower LUMO energy level of approximately −3.85 eV than that of the $CH_3NH_3PbI_3$ perovskite (−3.9 eV), which could induce a small charge extraction barrier when attaching the perovskite, delivering a reduced efficiency.[124]

7.2 Fulleropyrrolidine derivatives

Several fulleropyrrolidine derivatives synthesized *via* a one-step 1,3-dipolar cycloaddition reaction (*i.e.*, the Prato reaction) were demonstrated to be efficient ETLs applied in PSCs as well. In 2016, Echegoyen *et al.* synthesized two fullerene derivatives including 2,5-(dimethyl ester) C_{60} fulleropyrrolidine ($DMEC_{60}$) and the analogous C_{70} derivative ($DMEC_{70}$, Fig. 15) and applied them as ETLs to replace the $PC_{61}BM$ ETL in inverted PSCs. Due to the suitable LUMO energy level and higher electron mobility as well as the excellent electron extraction capability resulted from the interactions between the $CH_3NH_3PbI_3$ perovskite and the addend groups on fullerene derivatives, the devices based on $DMEC_{60}$ and $DMEC_{70}$ ETLs exhibited improved PCEs of 15.2% and 16.4%, respectively, which are both higher than those of devices based on $PC_{61}BM$ ETLs (14.5%) and $PC_{71}BM$ ETLs (15.0%).[125] Later on, Han *et al.* synthesized a high-symmetric bis-adduct of $DMEC_{60}$ (bis-$DMEC_{60}$, Fig. 15) and incorporated it into printable mesoscopic PSCs, achieving an improved PCE of 15.21% with negligible hysteresis relative to that of the control device without bis-$DMEC_{60}$ (13.01%). The strong chemical interaction between the perovskite and the incorporated bis-$DMEC_{60}$ improves the conductivity of the $(5\text{-AVA})_{0.03}(MA)_{0.97}PbI_3$ perovskite film and facilitates the defect passivation at the grain boundaries effectively.[126] In 2018, Khadka *et al.* developed an approach to tailor the performance of wide-band-gap $CH_3NH_3PbI_{3-x}Br_x$ PSCs with highly crystalline fulleropyrrolidine derivatives ($C_{60}MC_{12}$, Fig. 15). Compared to the amorphous $PC_{61}BM$, the higher crystallinity of long-chain alkyl-substituted $C_{60}MC_{12}$ is beneficial for mitigating the energy disorder (Fig. 16b) and soothing the recombination activities, contributing to the improved PCE of 16.74% and a high V_{oc} of 1.24 V.[47] More recently, Wei *et al.* applied 2,5-diphenyl C_{60} fulleropyrrolidine (DPC_{60}) as a modification layer sandwiched between SnO_2 and the $Cs_{0.05}(MA_{0.17}FA_{0.83})_{0.95}Pb(I_{0.83}Br_{0.17})_3$ perovskite in planar n–i–p PSCs, achieving a PCE of 20.4% along with excellent photothermal stability (Fig. 16c). The enhanced performance of PSCs is obtained from the inserted DPC_{60} interlayer that affords appropriate energy levels, and the improved electron mobility of the DPC_{60} film is due to the short distance between two adjacent fullerene cages, the chemical interaction with the perovskite layer, and low solubility in the perovskite solvents. Besides, the chemical interaction between N–H and I at the DPC_{60}/perovskite interface endowed the PSCs with enhanced defect passivation and reduced charge recombination. Furthermore, the smooth and hydrophobic DPC_{60} layer helps to reduce heterogeneous nucleation and to improve the perovskite film quality, resulting in excellent photothermal stability.[127] A similar high-symmetry fulleropyrrolidine derivative such as C_{60} pyrrolidine tris-acid ethyl ester (CPTA-E, Fig. 15) was applied as an ETL in planar p–i–n PSCs by Fang *et al.* The strong chemical interaction between CPTA-E and the perovskite through the coordination interaction of carboxylic ester groups with Pb^{2+} ions enhances the adhesion of CPTA-E on the surface of $CH_3NH_3PbI_3$, facilitating the formation of a uniform and full covering ETL which prevents the direct contact of the perovskite and metal electrodes. As a result, the device delivered a PCE of 17.44% with suppressed hysteresis and prolonged stability due to the reduced charge recombination at the perovskite/electrode interface.[128] More recently, Yang *et al.* synthesized a novel fulleropyrrolidine derivative bearing perylene diimide (PDI-C_{60}, Fig. 15) and used it as an ETL in inverted PSCs. Attaching the PDI group with large conductivity and high mobility onto the C_{60} cage enables the PDI-C_{60} ETL to possess a more matched energy level with the $CH_3NH_3PbI_3$ perovskite, more efficient charge extraction/transport and reduced recombination rate. Therefore, the devices based on PDI-C_{60} ETLs and PDI-C_{60} interlayers exhibit high PCEs of 18.6% and 20.2%, respectively (Fig. 16d). Furthermore, the better device stability after incorporating the PDI-C_{60} ETL results from the higher hydrophobic properties of PDI-C_{60}.[129]

7.3 Dimeric fullerene derivatives

All of the abovementioned fullerene derivatives are mostly based on monoadducts and bisadducts of the monomeric fullerene cage. Alternatively, several dimeric fullerene derivatives have also been applied as ETLs in p–i–n PSCs to improve the device performance and stability simultaneously. In 2016, Ai *et al.* prepared a dumb-belled $PC_{61}BM$ dimer (d-$PC_{61}BM$, Fig. 15) which was blended with $PC_{61}BM$ to form a hybrid ETL. Subsequently, the d-$PC_{61}BM$/$PC_{61}BM$ blend ETL with an optimized ratio of $PC_{61}BM$: d-$PC_{61}BM$ = 4 : 1 showed the capability of decreasing charge recombination, improving electron extraction, and adjusting the ETL morphology and $CH_3NH_3PbI_{3-x}Cl_x$ perovskite/ETL interface. As a result, the p–i–n PSCs with d-$PC_{61}BM$/$PC_{61}BM$ blended ETLs exhibited a PCE of 11.43%, which is higher than that of the control device based on the $PC_{61}BM$ ETL (10.34%).[130] Likewise, Echegoyen *et al.* synthesized an analogous dimeric fullerene derivative (D-C_{60}, Fig. 15) in 2017, in which two $PC_{61}BM$ moieties were linked together through the bridge molecule of 2,2-diethyl-1,3-propanediol. D-C_{60} was applied as the ETL in planar p–i–n $CH_3NH_3PbI_3$ PSCs, leading to a PCE of 16.6%, which is obviously higher than that of the control device with the $PC_{61}BM$ ETL (14.7%). The D-C_{60} ETL shows several advantages such as appropriate energy

levels, high electron mobility and easy solution processability. Furthermore, D-C_{60} can form a more hydrophobic and compact layer, which is beneficial for the improved device stability.[131]

8. Summary and outlook

During the rapid evolution of PSCs, fullerene derivatives with high electron affinity and strong electron accepting ability have played a crucial role in improving both the device performance and stability. Although the pristine fullerenes such as C_{60} and C_{70} possess strong electron extraction and electron transport ability, their relatively low solubilities in organic solvents limit applications in PSCs. Fortunately, functionalized fullerene derivatives have improved solubilities due to the grafting of the functional groups; thus they have been widely utilized in PSCs by means of being incorporated as interfacial materials between the perovskite layer and the electrode or as additives within the perovskite layer. As reviewed elaborately here, so far versatile functional groups, including polar groups (amino-, oligoether- and crown-ether), heterocyclic groups (pyridine and thiophene), the carboxyl (–COOH) group, the hydroxyl (–OH) group and halogen atoms, have been successfully grafted onto fullerene cages, affording a series of novel mono- or bis-adducts of fullerene derivatives, which have been extensively applied as either interlayers or additives in PSCs. In particular, unique fullerene derivatives bearing the cross-linkable groups (styryl and epoxy groups) can form insoluble cross-linked fullerene networks, and this enables the suppression of the wash away of the fullerene derivative ETL from DMF solvents during the process of perovskite precursor deposition. Besides, such fullerene derivatives have been incorporated as additives into PSCs and crosslinked into the insoluble network at the perovskite grain boundaries, contributing to improved device performance and stability. Moreover, with judicious molecular designs, fullerene derivatives with the perfect combination of the functional groups and fullerene cages may enable a reduced work function of metal cathodes, enhanced charge extraction/transfer, improved trap state/defect passivation and prolonged device stability.

Developing novel fullerene derivatives for further improving the device efficiency and stability of PSCs is still highly desirable yet challenging, because of the difficulty in the precise control on high-selectivity grafting of the suitable functional groups and their addition patterns, which are nevertheless critical and required for their high performance in PSCs. In addition, the in-depth mechanistic understanding of the correlation between the chemical structures of fullerene derivatives especially the functional groups and their effects on each photovoltaic parameter of PSCs is still needed, which can undoubtedly guide the design of novel fullerene derivatives. In particular, Lewis base functionalized fullerene derivatives especially those based on heterocyclic pyridine and thiophene moieties may render strong coordination interactions with Pb^{2+} ions of the perovskite, thus leading to effective passivation of the trap states and promoted charge transport. An intriguing question is whether other heterocyclic groups such as furan, imidazole, thiazole, or triazine can afford even stronger interactions with the perovskite or not. In addition, given that the fullerene cage is highly adjustable and the electronic properties of fullerenes can be readily tailored by varying their cage size or endohedral species,[132] other types of fullerenes with larger cage size and endohedral fullerenes can be utilized to construct novel fullerene derivatives with suitable energy levels and interactions with the perovskite and/or metal oxide layers. Furthermore, the structural tunability of fullerene derivatives promises their potential applications in large-area or flexible PSCs.

Conflicts of interest

There are no conflicts to declare.

Acknowledgements

This work was partially supported by the National Key Research and Development Program of China (2017YFA0402800) and the National Natural Science Foundation of China (51925206 and U1932214).

References

1 Y. Liu and Y. Chen, Integrated Perovskite/Bulk-Heterojunction Organic Solar Cells, *Adv. Mater.*, 2020, **32**, 1805843.
2 A. Mahapatra, D. Prochowicz, M. M. Tavakoli, S. Trivedi, P. Kumar and P. Yadav, A review of aspects of additive engineering in perovskite solar cells, *J. Mater. Chem. A*, 2020, **8**, 27–54.
3 H. Hu, M. Singh, X. Wan, J. Tang, C.-W. Chu and G. Li, Nucleation and crystal growth control for scalable solution-processed organic-inorganic hybrid perovskite solar cells, *J. Mater. Chem. A*, 2020, **8**, 1578–1603.
4 Z. Hu, Z. Lin, J. Su, J. Zhang, J. Chang and Y. Hao, A Review on Energy Band-Gap Engineering for Perovskite Photovoltaics, *Sol. RRL*, 2019, **3**, 1900304.
5 T. Hwang, B. Lee, J. Kim, S. Lee, B. Gil, A. J. Yun and B. Park, From Nanostructural Evolution to Dynamic Interplay of Constituents: Perspectives for Perovskite Solar Cells, *Adv. Mater.*, 2018, **30**, e1704208.
6 L.-L. Deng, S.-Y. Xie and F. Gao, Fullerene-Based Materials for Photovoltaic Applications: Toward Efficient, Hysteresis-Free, and Stable Perovskite Solar Cells, *Adv. Electron. Mater.*, 2018, **4**, 1700435.
7 H. Zhou, Q. Chen, G. Li, S. Luo, T.-b. Song, H.-S. Duan, Z. Hong, J. You, Y. Liu and Y. Yang, Interface engineering of highly efficient perovskite solar cells, *Science*, 2014, **345**, 542–546.
8 A. Kojima, K. Teshima, Y. Shirai and T. Miyasaka, Organometal Halide Perovskites as Visible-Light Sensitizers for Photovoltaic Cells, *J. Am. Chem. Soc.*, 2009, **131**, 6050–6051.

9 Research cell efficiency records, https://www.nrel.gov/pv/assets/pdfs/best-research-cell-efficiencies.20200406.pdf (National Renewable Energy Laboratory).
10 W. Hu, W. Zhou, X. Lei, P. Zhou, M. Zhang, T. Chen, H. Zeng, J. Zhu, S. Dai, S. Yang and S. Yang, Low-Temperature In Situ Amino Functionalization of TiO_2 Nanoparticles Sharpens Electron Management Achieving over 21% Efficient Planar Perovskite Solar Cells, *Adv. Mater.*, 2019, **31**, e1806095.
11 D. Luo, R. Su, W. Zhang, Q. Gong and R. Zhu, Minimizing non-radiative recombination losses in perovskite solar cells, *Nat. Rev. Chem.*, 2020, **5**, 44–60.
12 Y. Zhou, X. Li and H. Lin, To Be Higher and Stronger-Metal Oxide Electron Transport Materials for Perovskite Solar Cells, *Small*, 2020, **16**, 1902579.
13 F. Zhang and K. Zhu, Additive Engineering for Efficient and Stable Perovskite Solar Cells, *Adv. Energy Mater.*, 2019, **9**, 1902579.
14 E. Castro, J. Murillo, O. Fernandez-Delgado and L. Echegoyen, Progress in fullerene-based hybrid perovskite solar cells, *J. Mater. Chem. C*, 2018, **6**, 2635–2651.
15 T. Umeyama and H. Imahori, A chemical approach to perovskite solar cells: control of electron-transporting mesoporous TiO_2 and utilization of nanocarbon materials, *Dalton Trans.*, 2017, **46**, 15615–15627.
16 A. Mahapatra, D. Prochowicz, M. M. Tavakoli, S. Trivedi, P. Kumar and P. Yadav, A review of aspects of additive engineering in perovskite solar cells, *J. Mater. Chem. A*, 2020, **8**, 27–54.
17 M. Jung, S.-G. Ji, G. Kim and S. I. Seok, Perovskite precursor solution chemistry: from fundamentals to photovoltaic applications, *Chem. Soc. Rev.*, 2019, **48**, 2011–2038.
18 N. J. Jeon, J. H. Noh, Y. C. Kim, W. S. Yang, S. Ryu and S. I. Seok, Solvent engineering for high-performance inorganic-organic hybrid perovskite solar cells, *Nat. Mater.*, 2014, **13**, 897–903.
19 H. Zhang, M. K. Nazeeruddin and W. C. H. Choy, Perovskite Photovoltaics: The Significant Role of Ligands in Film Formation, Passivation, and Stability, *Adv. Mater.*, 2019, **31**, 1805702.
20 W. Hu, S. Yang and S. Yang, Surface Modification of TiO_2 for Perovskite Solar Cells, *Trends Chem.*, 2020, **2**, 148–162.
21 F. Gao, Y. Zhao, X. Zhang and J. You, Recent Progresses on Defect Passivation toward Efficient Perovskite Solar Cells, *Adv. Energy Mater.*, 2019, **9**, 1902650.
22 A. Rajagopal, K. Yao and A. K.-Y. Jen, Toward Perovskite Solar Cell Commercialization: A Perspective and Research Roadmap Based on Interfacial Engineering, *Adv. Mater.*, 2018, **30**, e1800455.
23 W. Deng, X. Liang, P. S. Kubiak and P. J. Cameron, Molecular Interlayers in Hybrid Perovskite Solar Cells, *Adv. Energy Mater.*, 2018, **8**, 1701544.
24 C. Liu, Y.-B. Cheng and Z. Ge, Understanding of perovskite crystal growth and film formation in scalable deposition processes, *Chem. Soc. Rev.*, 2020, **49**, 1653–1687.
25 S. Liu, Y. Guan, Y. Sheng, Y. Hu, Y. Rong, A. Mei and H. Han, A Review on Additives for Halide Perovskite Solar Cells, *Adv. Energy Mater.*, 2019, **9**, 1902492.
26 C. Cui, Y. Li and Y. Li, Fullerene Derivatives for the Applications as Acceptor and Cathode Buffer Layer Materials for Organic and Perovskite Solar Cells, *Adv. Energy Mater.*, 2017, **7**, 1601251.
27 J. Zhen, W. Zhou, M. Chen, B. Li, L. Jia, M. Wang and S. Yang, Pyridine-functionalized fullerene additive enabling coordination interactions with $CH_3NH_3PbI_3$ perovskite towards highly efficient bulk heterojunction solar cells, *J. Mater. Chem. A*, 2019, **7**, 2754–2763.
28 J. Xu, A. Buin, A. H. Ip, W. Li, O. Voznyy, R. Comin, M. Yuan, S. Jeon, Z. Ning and J. J. McDowell, Perovskite-fullerene hybrid materials suppress hysteresis in planar diodes, *Nat. Commun.*, 2015, **6**, 1–8.
29 Y. Shao, Y. Fang, T. Li, Q. Wang, Q. Dong, Y. Deng, Y. Yuan, H. Wei, M. Wang and A. Gruverman, Grain boundary dominated ion migration in polycrystalline organic-inorganic halide perovskite films, *Energy Environ. Sci.*, 2016, **9**, 1752–1759.
30 T. Umeyama and H. Imahori, Isomer Effects of Fullerene Derivatives on Organic Photovoltaics and Perovskite Solar Cells, *Acc. Chem. Res.*, 2019, **52**, 2046–2055.
31 Y. Fang, C. Bi, D. Wang and J. Huang, The Functions of Fullerenes in Hybrid Perovskite Solar Cells, *ACS Energy Lett.*, 2017, **2**, 782–794.
32 M. A. Kumari, T. Swetha and S. P. Singh, Fullerene derivatives: A review on perovskite solar cells, *Mater. Express*, 2018, **8**, 389–406.
33 J. Y. Jeng, Y. F. Chiang, M. H. Lee, S. R. Peng, T. F. Guo, P. Chen and T. C. Wen, $CH_3NH_3PbI_3$ perovskite/fullerene planar-heterojunction hybrid solar cells, *Adv. Mater.*, 2013, **25**, 3727–3732.
34 Y. Shao, Z. Xiao, C. Bi, Y. Yuan and J. Huang, Origin and elimination of photocurrent hysteresis by fullerene passivation in $CH_3NH_3PbI_3$ planar heterojunction solar cells, *Nat. Commun.*, 2014, **5**, 5784.
35 Y. Shao, Y. Yuan and J. Huang, Correlation of energy disorder and open-circuit voltage in hybrid perovskite solar cells, *Nat. Energy*, 2016, **1**, 1–6.
36 W. Nie, H. Tsai, R. Asadpour, J.-C. Blancon, A. J. Neukirch, G. Gupta, J. J. Crochet, M. Chhowalla, S. Tretiak and M. A. Alam, High-efficiency solution-processed perovskite solar cells with millimeter-scale grains, *Science*, 2015, **347**, 522–525.
37 J. H. Heo, H. J. Han, D. Kim, T. K. Ahn and S. H. Im, Hysteresis-less inverted $CH_3NH_3PbI_3$ planar perovskite hybrid solar cells with 18.1% power conversion efficiency, *Energy Environ. Sci.*, 2015, **8**, 1602–1608.
38 Q. Wang, Y. Shao, Q. Dong, Z. Xiao, Y. Yuan and J. Huang, Large fill-factor bilayer iodine perovskite solar cells fabricated by a low-temperature solution-process, *Energy Environ. Sci.*, 2014, **7**, 2359–2365.
39 C.-H. Chiang, Z.-L. Tseng and C.-G. Wu, Planar heterojunction perovskite/$PC_{71}BM$ solar cells with enhanced open-circuit voltage *via* a (2/1)-step spin-coating process, *J. Mater. Chem. A*, 2014, **2**, 15897–15903.
40 S.-M. Dai, X. Zhang, W.-Y. Chen, X. Li, Z. a. Tan, C. Li, L.-L. Deng, X.-X. Zhan, M.-S. Lin, Z. Xing and S.-Y. Xie,

Formulation engineering for optimizing ternary electron acceptors exemplified by isomeric $PC_{71}BM$ in planar perovskite solar cells, *J. Mater. Chem. A*, 2016, **4**, 18776–18782.
41 C. Liu, K. Wang, P. Du, C. Yi, T. Meng and X. Gong, Efficient Solution-Processed Bulk Heterojunction Perovskite Hybrid Solar Cells, *Adv. Energy Mater.*, 2015, **5**, 1402024.
42 C.-H. Chiang and C.-G. Wu, Bulk heterojunction perovskite-PCBM solar cells with high fill factor, *Nat. Photonics*, 2016, **10**, 196–200.
43 C. Park, H. Ko, D. H. Sin, K. C. Song and K. Cho, Organometal Halide Perovskite Solar Cells with Improved Thermal Stability *via* Grain Boundary Passivation Using a Molecular Additive, *Adv. Funct. Mater.*, 2017, **27**, 1703546.
44 Y. Wu, X. Yang, W. Chen, Y. Yue, M. Cai, F. Xie, E. Bi, A. Islam and L. Han, Perovskite solar cells with 18.21% efficiency and area over 1 cm^2 fabricated by heterojunction engineering, *Nat. Energy*, 2016, **1**, 16148.
45 F. Zhang, W. Shi, J. Luo, N. Pellet, C. Yi, X. Li, X. Zhao, T. J. S. Dennis, X. Li, S. Wang, Y. Xiao, S. M. Zakeeruddin, D. Bi and M. Gratzel, Isomer-Pure Bis-PCBM-Assisted Crystal Engineering of Perovskite Solar Cells Showing Excellent Efficiency and Stability, *Adv. Mater.*, 2017, **29**, 1606806.
46 L. Gil-Escrig, C. Momblona, M. Sessolo and H. J. Bolink, Fullerene imposed high open-circuit voltage in efficient perovskite based solar cells, *J. Mater. Chem. A*, 2016, **4**, 3667–3672.
47 D. B. Khadka, Y. Shirai, M. Yanagida, T. Noda and K. Miyano, Tailoring the Open-Circuit Voltage Deficit of Wide-Band-Gap Perovskite Solar Cells Using Alkyl Chain-Substituted Fullerene Derivatives, *ACS Appl. Mater. Interfaces*, 2018, **10**, 22074–22082.
48 M. Elnaggar, M. Elshobaki, A. Mumyatov, S. Y. Luchkin, N. N. Dremova, K. J. Stevenson and P. A. Troshin, Molecular Engineering of the Fullerene-Based Electron Transport Layer Materials for Improving Ambient Stability of Perovskite Solar Cells, *Sol. RRL*, 2019, **3**, 1900223.
49 C. Tian, E. Castro, G. Betancourt-Solis, Z. Nan, O. Fernandez-Delgado, S. Jankuru and L. Echegoyen, Fullerene derivative with a branched alkyl chain exhibits enhanced charge extraction and stability in inverted planar perovskite solar cells, *New J. Chem.*, 2018, **42**, 2896–2902.
50 Q.-H. Zhang, W.-D. Hu, X.-F. Wang, G. Chen, J.-P. Zhang, L.-X. Xiao and T. Miyasaka, Fullerene Multiadducts as Electron Collection Layers for Perovskite Solar Cells, *Chem. Lett.*, 2017, **46**, 101–103.
51 C.-Z. Li, P.-W. Liang, D. B. Sulas, P. D. Nguyen, X. Li, D. S. Ginger, C. W. Schlenker and A. K.-Y. Jen, Modulation of hybrid organic-perovskite photovoltaic performance by controlling the excited dynamics of fullerenes, *Mater. Horiz.*, 2015, **2**, 414–419.
52 Q. Dong, C. H. Y. Ho, H. Yu, A. Salehi and F. So, Defect passivation by fullerene derivative in perovskite solar cells with aluminum-doped zinc oxide as electron transporting layer, *Chem. Mater.*, 2019, **31**, 6833–6840.
53 Y. Li, Y. Zhao, Q. Chen, Y. M. Yang, Y. Liu, Z. Hong, Z. Liu, Y. T. Hsieh, L. Meng, Y. Li and Y. Yang, Multifunctional Fullerene Derivative for Interface Engineering in Perovskite Solar Cells, *J. Am. Chem. Soc.*, 2015, **137**, 15540–15547.
54 L. Meng, J. You, T. F. Guo and Y. Yang, Recent Advances in the Inverted Planar Structure of Perovskite Solar Cells, *Acc. Chem. Res.*, 2016, **49**, 155–165.
55 H. Azimi, T. Ameri, H. Zhang, Y. Hou, C. O. R. Quiroz, J. Min, M. Hu, Z.-G. Zhang, T. Przybilla, G. J. Matt, E. Spiecker, Y. Li and C. J. Brabec, A Universal Interface Layer Based on an Amine-Functionalized Fullerene Derivative with Dual Functionality for Efficient Solution Processed Organic and Perovskite Solar Cells, *Adv. Energy Mater.*, 2015, **5**, 1401692.
56 Y. Liu, M. Bag, L. A. Renna, Z. A. Page, P. Kim, T. Emrick, D. Venkataraman and T. P. Russell, Understanding Interface Engineering for High-Performance Fullerene/Perovskite Planar Heterojunction Solar Cells, *Adv. Energy Mater.*, 2016, **6**, 1501606.
57 J. Xie, X. Yu, X. Sun, J. Huang, Y. Zhang, M. Lei, K. Huang, D. Xu, Z. Tang, C. Cui and D. Yang, Improved performance and air stability of planar perovskite solar cells *via* interfacial engineering using a fullerene amine interlayer, *Nano Energy*, 2016, **28**, 330–337.
58 Y. Zhang, P. Wang, X. Yu, J. Xie, X. Sun, H. Wang, J. Huang, L. Xu, C. Cui, M. Lei and D. Yang, Enhanced performance and light soaking stability of planar perovskite solar cells using an amine-based fullerene interfacial modifier, *J. Mater. Chem. A*, 2016, **4**, 18509–18515.
59 J. Xie, X. Yu, J. Huang, X. Sun, Y. Zhang, Z. Yang, M. Lei, L. Xu, Z. Tang, C. Cui, P. Wang and D. Yang, Self-Organized Fullerene Interfacial Layer for Efficient and Low-Temperature Processed Planar Perovskite Solar Cells with High UV-Light Stability, *Adv. Sci.*, 2017, **4**, 1700018.
60 X. Liu, P. Huang, Q. Dong, Z. Wang, K. Zhang, H. Yu, M. Lei, Y. Zhou, B. Song and Y. Li, Enhancement of the efficiency and stability of planar p–i–n perovskite solar cells *via* incorporation of an amine-modified fullerene derivative as a cathode buffer layer, *Sci. China: Chem.*, 2016, **60**, 136–143.
61 L. Jia, B. Li, Y. Shang, M. Chen, G.-W. Wang and S. Yang, Double fullerene cathode buffer layers afford highly efficient and stable inverted planar perovskite solar cells, *Org. Electron.*, 2020, **82**, 105726.
62 Q. Chen, W. Wang, S. Xiao, Y. B. Cheng, F. Huang and W. Xiang, Improved Performance of Planar Perovskite Solar Cells Using an Amino-Terminated Multifunctional Fullerene Derivative as the Passivation Layer, *ACS Appl. Mater. Interfaces*, 2019, **11**, 27145–27152.
63 S. Wang, H. Chen, J. Zhang, G. Xu, W. Chen, R. Xue, M. Zhang, Y. Li and Y. Li, Targeted Therapy for Interfacial Engineering Toward Stable and Efficient Perovskite Solar Cells, *Adv. Mater.*, 2019, **31**, e1903691.
64 M. Zhang, Q. Chen, R. Xue, Y. Zhan, C. Wang, J. Lai, J. Yang, H. Lin, J. Yao, Y. Li, L. Chen and Y. Li, Reconfiguration of interfacial energy band structure for high-performance inverted structure perovskite solar cells, *Nat. Commun.*, 2019, **10**, 4593.
65 P. W. Liang, C. Y. Liao, C. C. Chueh, F. Zuo, S. T. Williams, X. K. Xin, J. Lin and A. K.-Y. Jen, Additive enhanced

crystallization of solution-processed perovskite for highly efficient planar-heterojunction solar cells, *Adv. Mater.*, 2014, **26**, 3748–3754.

66 K. Yan, Z.-X. Liu, X. Li, J. Chen, H. Chen and C.-Z. Li, Conductive fullerene surfactants *via* anion doping as cathode interlayers for efficient organic and perovskite solar cells, *Org. Chem. Front.*, 2018, **5**, 2845–2851.

67 S. Shao, M. Abdu-Aguye, L. Qiu, L.-H. Lai, J. Liu, S. Adjokatse, F. Jahani, M. E. Kamminga, G. H. ten Brink, T. T. M. Palstra, B. J. Kooi, J. C. Hummelen and M. Antonietta Loi, Elimination of the light soaking effect and performance enhancement in perovskite solar cells using a fullerene derivative, *Energy Environ. Sci.*, 2016, **9**, 2444–2452.

68 Y. Xing, C. Sun, H. L. Yip, G. C. Bazan, F. Huang and Y. Cao, New fullerene design enables efficient passivation of surface traps in high performance p–i–n heterojunction perovskite solar cells, *Nano Energy*, 2016, **26**, 7–15.

69 K. Yan, J. Chen, H. Ju, F. Ding, H. Chen and C.-Z. Li, Achieving high-performance thick-film perovskite solar cells with electron transporting Bingel fullerenes, *J. Mater. Chem. A*, 2018, **6**, 15495–15503.

70 G. Xu, R. Xue, W. Chen, J. Zhang, M. Zhang, H. Chen, C. Cui, H. Li, Y. Li and Y. Li, New Strategy for Two-Step Sequential Deposition: Incorporation of Hydrophilic Fullerene in Second Precursor for High-Performance p–i–n Planar Perovskite Solar Cells, *Adv. Energy Mater.*, 2018, **8**, 1703054.

71 G. Xu, S. Wang, P. Bi, H. Chen, M. Zhang, R. Xue, X. Hao, Z. Wang, Y. Li and Y. Li, Hydrophilic Fullerene Derivative Doping in Active Layer and Electron Transport Layer for Enhancing Oxygen Stability of Perovskite Solar Cells, *Sol. RRL*, 2019, **9**, 1900249.

72 X. Liu, W. Jiao, M. Lei, Y. Zhou, B. Song and Y. Li, Crown-ether functionalized fullerene as a solution-processable cathode buffer layer for high performance perovskite and polymer solar cells, *J. Mater. Chem. A*, 2015, **3**, 9278–9284.

73 X. Liu, M. Lei, Y. Zhou, B. Song and Y. Li, High performance planar p–i–n perovskite solar cells with crown-ether functionalized fullerene and LiF as double cathode buffer layers, *Appl. Phys. Lett.*, 2015, **107**, 063901.

74 S. Collavini, M. Saliba, W. R. Tress, P. J. Holzhey, S. F. Volker, K. Domanski, S. H. Turren-Cruz, A. Ummadisingu, S. M. Zakeeruddin, A. Hagfeldt, M. Gratzel and J. L. Delgado, Poly(ethylene glycol)-[60]Fullerene-Based Materials for Perovskite Solar Cells with Improved Moisture Resistance and Reduced Hysteresis, *ChemSusChem*, 2018, **11**, 1032–1039.

75 Q. Qin, Z. Zhang, Y. Cai, Y. Zhou, H. Liu, X. Lu, X. Gao, L. Shui, S. Wu and J. Liu, Improving the performance of low-temperature planar perovskite solar cells by adding functional fullerene end-capped polyethylene glycol derivatives, *J. Power Sources*, 2018, **396**, 49–56.

76 Q. Fu, S. Xiao, X. Tang, Y. Chen and T. Hu, Amphiphilic Fullerenes Employed to Improve the Quality of Perovskite Films and the Stability of Perovskite Solar Cells, *ACS Appl. Mater. Interfaces*, 2019, **11**, 24782–24788.

77 N. K. Noel, A. Abate, S. D. Stranks, E. S. Parrott, V. M. Burlakov, A. Goriely and H. J. Snaith, Enhanced Photoluminescence and Solar Cell Performance *via* Lewis Base Passivation of OrganicInorganic Lead Halide Perovskites, *ACS Nano*, 2014, **8**, 9815–9821.

78 B. Li, J. Zhen, Y. Wan, X. Lei, Q. Liu, Y. Liu, L. Jia, X. Wu, H. Zeng, W. Zhang, G. W. Wang, M. Chen and S. Yang, Anchoring Fullerene onto Perovskite Film *via* Grafting Pyridine toward Enhanced Electron Transport in High-Efficiency Solar Cells, *ACS Appl. Mater. Interfaces*, 2018, **10**, 32471–32482.

79 B. Li, J. Zhen, Y. Wan, X. Lei, L. Jia, X. Wu, H. Zeng, M. Chen, G.-W. Wang and S. Yang, Steering the electron transport properties of pyridine-functionalized fullerene derivatives in inverted perovskite solar cells: the nitrogen site matters, *J. Mater. Chem. A*, 2020, **8**, 3872–3881.

80 H. R. Liu, S. H. Li, L. L. Deng, Z. Y. Wang, Z. Xing, X. Rong, H. R. Tian, X. Li, S. Y. Xie, R. B. Huang and L. S. Zheng, Pyridine-Functionalized Fullerene Electron Transport Layer for Efficient Planar Perovskite Solar Cells, *ACS Appl. Mater. Interfaces*, 2019, **11**, 23982–23989.

81 E. Castro, O. Fernandez-Delgado, F. Arslan, G. Zavala, T. Yang, S. Seetharaman, F. Souza and L. Echegoyen, New thiophene-based C_{60} fullerene derivatives as efficient electron transporting materials for perovskite solar cells, *New J. Chem.*, 2018, **42**, 14551–14558.

82 O. Fernandez-Delgado, E. Castro, C. R. Ganivet, K. Fosnacht, F. Liu, T. Mates, Y. Liu, X. Wu and L. Echegoyen, Variation of Interfacial Interactions in $PC_{61}BM$-like Electron-Transporting Compounds for Perovskite Solar Cells, *ACS Appl. Mater. Interfaces*, 2019, **11**, 34408–34415.

83 E. Castro, O. Fernandez-Delgado, A. Artigas, G. Zavala, F. Liu, A. Moreno-Vicente, A. Rodríguez-Fortea, J. D. Velasquez, J. M. Poblet and L. Echegoyen, α-DTC_{70} fullerene performs significantly better than β-DTC_{70} as electron transporting material in perovskite solar cells, *J. Mater. Chem. C*, 2020, **8**, 6813–6819.

84 K. Liu, S. Chen, J. Wu, H. Zhang, M. Qin, X. Lu, Y. Tu, Q. Meng and X. Zhan, Fullerene derivative anchored SnO_2 for high-performance perovskite solar cells, *Energy Environ. Sci.*, 2018, **11**, 3463–3471.

85 A. Abrusci, S. D. Stranks, P. Docampo, H. L. Yip, A. K.-Y. Jen and H. J. Snaith, High-performance perovskite-polymer hybrid solar cells *via* electronic coupling with fullerene monolayers, *Nano Lett.*, 2013, **13**, 3124–3128.

86 K. Wojciechowski, S. D. Stranks, A. Abate, G. Sadoughi, A. Sadhanala, N. Kopidakis, G. Rumbles, C.-Z. Li, R. H. Friend and A. K.-Y. Jen, Heterojunction modification for highly efficient organic-inorganic perovskite solar cells, *ACS Nano*, 2014, **8**, 12701–12709.

87 M. Valles-Pelarda, B. C. Hames, I. Garcia-Benito, O. Almora, A. Molina-Ontoria, R. S. Sanchez, G. Garcia-Belmonte, N. Martin and I. Mora-Sero, Analysis of the Hysteresis Behavior of Perovskite Solar Cells with Interfacial Fullerene Self-Assembled Monolayers, *J. Phys. Chem. Lett.*, 2016, **7**, 4622–4628.

88 Y. Bai, Q. Dong, Y. Shao, Y. Deng, Q. Wang, L. Shen, D. Wang, W. Wei and J. Huang, Enhancing stability and efficiency of perovskite solar cells with crosslinkable silane-functionalized and doped fullerene, *Nat. Commun.*, 2016, **7**, 12806.

89 Y. Dong, W. Li, X. Zhang, Q. Xu, Q. Liu, C. Li and Z. Bo, Highly efficient planar perovskite solar cells *via* interfacial modification with fullerene derivatives, *Small*, 2016, **12**, 1098–1104.

90 K. Wang, C. Liu, P. Du, J. Zheng and X. Gong, Bulk heterojunction perovskite hybrid solar cells with large fill factor, *Energy Environ. Sci.*, 2015, **8**, 1245–1255.

91 C. Liu, K. Wang, P. Du, T. Meng, X. Yu, S. Z. Cheng and X. Gong, High performance planar heterojunction perovskite solar cells with fullerene derivatives as the electron transport layer, *ACS Appl. Mater. Interfaces*, 2015, **7**, 1153–1159.

92 Y.-C. Wang, X. Li, L. Zhu, X. Liu, W. Zhang and J. Fang, Efficient and Hysteresis-Free Perovskite Solar Cells Based on a Solution Processable Polar Fullerene Electron Transport Layer, *Adv. Energy Mater.*, 2017, **7**, 1701144.

93 M. Zhong, Y. Liang, J. Zhang, Z. Wei, Q. Li and D. Xu, Highly efficient flexible $MAPbI_3$ solar cells with a fullerene derivative-modified SnO_2 layer as the electron transport layer, *J. Mater. Chem. A*, 2019, **7**, 6659–6664.

94 Z. Yang, M. Zhong, Y. Liang, L. Yang, X. Liu, Q. Li, J. Zhang and D. Xu, SnO_2-C_{60} Pyrrolidine Tris-Acid (CPTA) as the Electron Transport Layer for Highly Efficient and Stable Planar Sn-Based Perovskite Solar Cells, *Adv. Funct. Mater.*, 2019, **29**, 1903621.

95 T. Cao, Z. Wang, Y. Xia, B. Song, Y. Zhou, N. Chen and Y. Li, Facilitating electron transportation in perovskite solar cells *via* water-soluble fullerenol interlayers, *ACS Appl. Mater. Interfaces*, 2016, **8**, 18284–18291.

96 T. Cao, P. Huang, K. Zhang, Z. Sun, K. Zhu, L. Yuan, K. Chen, N. Chen and Y. Li, Interfacial engineering *via* inserting functionalized water-soluble fullerene derivative interlayers for enhancing the performance of perovskite solar cells, *J. Mater. Chem. A*, 2018, **6**, 3435–3443.

97 W. Zhou, J. Zhen, Q. Liu, Z. Fang, D. Li, P. Zhou, T. Chen and S. Yang, Successive surface engineering of TiO_2 compact layers *via* dual modification of fullerene derivatives affording hysteresis-suppressed high-performance perovskite solar cells, *J. Mater. Chem. A*, 2017, **5**, 1724–1733.

98 T. Cao, K. Chen, Q. Chen, Y. Zhou, N. Chen and Y. Li, Fullerene Derivative-Modified SnO_2 Electron Transport Layer for Highly Efficient Perovskite Solar Cells with Efficiency over 21%, *ACS Appl. Mater. Interfaces*, 2019, **11**, 33825–33834.

99 K. Yao, S. Leng, Z. Liu, L. Fei, Y. Chen, S. Li, N. Zhou, J. Zhang, Y.-X. Xu, L. Zhou, H. Huang and A. K.-Y. Jen, Fullerene-Anchored Core-Shell ZnO Nanoparticles for Efficient and Stable Dual-Sensitized Perovskite Solar Cells, *Joule*, 2019, **3**, 417–431.

100 H. Wang, F. Cai, M. Zhang, P. Wang, J. Yao, R. S. Gurney, F. Li, D. Liu and T. Wang, Halogen-substituted fullerene derivatives for interface engineering of perovskite solar cells, *J. Mater. Chem. A*, 2018, **6**, 21368–21378.

101 D. Bi, P. Gao, R. Scopelliti, E. Oveisi, J. Luo, M. Grätzel, A. Hagfeldt and M. K. Nazeeruddin, High-Performance Perovskite Solar Cells with Enhanced Environmental Stability Based on Amphiphile-Modified $CH_3NH_3PbI_3$, *Adv. Mater.*, 2016, **28**, 2910–2915.

102 X. Liu, F. Lin, C.-C. Chueh, Q. Chen, T. Zhao, P.-W. Liang, Z. Zhu, Y. Sun and A. K.-Y. Jen, Fluoroalkyl-substituted fullerene/perovskite heterojunction for efficient and ambient stable perovskite solar cells, *Nano Energy*, 2016, **30**, 417–425.

103 A. Rajagopal, P.-W. Liang, C.-C. Chueh, Z. Yang and A. K. Y. Jen, Defect Passivation *via* a Graded Fullerene Heterojunction in Low-Bandgap Pb–Sn Binary Perovskite Photovoltaics, *ACS Energy Lett.*, 2017, **2**, 2531–2539.

104 Z. Zhu, C. C. Chueh, F. Lin and A. K.-Y. Jen, Enhanced Ambient Stability of Efficient Perovskite Solar Cells by Employing a Modified Fullerene Cathode Interlayer, *Adv. Sci.*, 2016, **3**, 1600027.

105 C.-Y. Chang, C.-P. Wang, R. Raja, L. Wang, C.-S. Tsao and W.-F. Su, High-efficiency bulk heterojunction perovskite solar cell fabricated by one-step solution process using single solvent: synthesis and characterization of material and film formation mechanism, *J. Mater. Chem. A*, 2018, **6**, 4179–4188.

106 R. Sandoval-Torrientes, J. Pascual, I. Garcia-Benito, S. Collavini, I. Kosta, R. Tena-Zaera, N. Martin and J. L. Delgado, Modified Fullerenes for Efficient Electron Transport Layer-Free Perovskite/Fullerene Blend-Based Solar Cells, *ChemSusChem*, 2017, **10**, 2023–2029.

107 K. Wojciechowski, I. Ramirez, T. Gorisse, O. Dautel, R. Dasari, N. Sakai, J. M. Hardigree, S. Song, S. Marder, M. Riede, G. Wantz and H. J. Snaith, Cross-Linkable Fullerene Derivatives for Solution-Processed n–i–p Perovskite Solar Cells, *ACS Energy Lett.*, 2016, **1**, 648–653.

108 M. Li, Y.-H. Chao, T. Kang, Z.-K. Wang, Y.-G. Yang, S.-L. Feng, Y. Hu, X.-Y. Gao, L.-S. Liao and C.-S. Hsu, Enhanced crystallization and stability of perovskites by a cross-linkable fullerene for high-performance solar cells, *J. Mater. Chem. A*, 2016, **4**, 15088–15094.

109 M. Li, Z.-K. Wang, T. Kang, Y. Yang, X. Gao, C.-S. Hsu, Y. Li and L.-S. Liao, Graphdiyne-modified cross-linkable fullerene as an efficient electron-transporting layer in organometal halide perovskite solar cells, *Nano Energy*, 2018, **43**, 47–54.

110 C. Tao, J. Van Der Velden, L. Cabau, N. F. Montcada, S. Neutzner, A. R. Srimath Kandada, S. Marras, L. Brambilla, M. Tommasini, W. Xu, R. Sorrentino, A. Perinot, M. Caironi, C. Bertarelli, E. Palomares and A. Petrozza, Fully Solution-Processed n–i–p-Like Perovskite Solar Cells with Planar Junction: How the Charge Extracting Layer Determines the Open-Circuit Voltage, *Adv. Mater.*, 2017, **29**, 1604493.

111 B. L. Watson, N. Rolston, K. A. Bush, T. Leijtens, M. D. McGehee and R. H. Dauskardt, Solvent-Resistant

Fullerene Contacts for Robust and Efficient Perovskite Solar Cells with Increased J_{sc} and V_{oc}, *ACS Appl. Mater. Interfaces*, 2016, **8**, 25896–25904.

112 T. Kang, C. M. Tsai, Y. H. Jiang, G. Gollavelli, N. Mohanta, E. W. Diau and C. S. Hsu, Interfacial Engineering with Cross-Linkable Fullerene Derivatives for High-Performance Perovskite Solar Cells, *ACS Appl. Mater. Interfaces*, 2017, **9**, 38530–38536.

113 M. Li, Y. G. Yang, Z. K. Wang, T. Kang, Q. Wang, S. H. Turren-Cruz, X. Y. Gao, C. S. Hsu, L. S. Liao and A. Abate, Perovskite Grains Embraced in a Soft Fullerene Network Make Highly Efficient Flexible Solar Cells with Superior Mechanical Stability, *Adv. Mater.*, 2019, **31**, e1901519.

114 W. Qiu, J. Bastos, S. Dasgupta, T. Merckx, I. Cardinaletti, M. Jenart, C. Nielsen, R. Gehlhaar, J. Poortmans and P. Heremans, Highly efficient perovskite solar cells with crosslinked PCBM interlayers, *J. Mater. Chem. A*, 2017, **5**, 2466–2472.

115 P. W. Liang, C. C. Chueh, S. T. Williams and A. K.-Y. Jen, Roles of fullerene-based interlayers in enhancing the performance of organometal perovskite thin-film solar cells, *Adv. Energy Mater.*, 2015, **5**, 1402321.

116 C.-G. Wu, C.-H. Chiang and S. H. Chang, A perovskite cell with a record-high-V_{oc} of 1.61 V based on solvent annealed $CH_3NH_3PbBr_3$/ICBA active layer, *Nanoscale*, 2016, **8**, 4077–4085.

117 Y. Lin, B. Chen, F. Zhao, X. Zheng, Y. Deng, Y. Shao, Y. Fang, Y. Bai, C. Wang and J. Huang, Matching Charge Extraction Contact for Wide-Bandgap Perovskite Solar Cells, *Adv. Mater.*, 2017, **29**, 1700607.

118 C. M. Wolff, F. Zu, A. Paulke, L. P. Toro, N. Koch and D. Neher, Reduced Interface-Mediated Recombination for High Open-Circuit Voltages in $CH_3NH_3PbI_3$ Solar Cells, *Adv. Mater.*, 2017, **29**, 1700159.

119 Q. Xue, Y. Bai, M. Liu, R. Xia, Z. Hu, Z. Chen, X.-F. Jiang, F. Huang, S. Yang, Y. Matsuo, H.-L. Yip and Y. Cao, Dual Interfacial Modifications Enable High Performance Semitransparent Perovskite Solar Cells with Large Open Circuit Voltage and Fill Factor, *Adv. Energy Mater.*, 2017, **7**, 1602333.

120 X. Meng, Y. Bai, S. Xiao, T. Zhang, C. Hu, Y. Yang, X. Zheng and S. Yang, Designing new fullerene derivatives as electron transporting materials for efficient perovskite solar cells with improved moisture resistance, *Nano Energy*, 2016, **30**, 341–346.

121 S.-M. Dai, L.-L. Deng, M.-L. Zhang, W.-Y. Chen, P. Zhu, X. Wang, C. Li, Z. a. Tan, S.-Y. Xie and R.-B. Huang, Two cyclohexanofullerenes used as electron transport materials in perovskite solar cells, *Inorg. Chim. Acta*, 2017, **468**, 146–151.

122 S. Chang, G. D. Han, J. G. Weis, H. Park, O. Hentz, Z. Zhao, T. M. Swager and S. Gradečak, Transition metal-oxide free perovskite solar cells enabled by a new organic charge transport layer, *ACS Appl. Mater. Interfaces*, 2016, **8**, 8511–8519.

123 T. Umeyama, D. Matano, S. Shibata, J. Baek, S. Ito and H. Imahori, Thermal Precursor Approach to Pristine Fullerene Film as Electron Selective Layer in Perovskite Solar Cells, *ECS J. Solid State Sci. Technol.*, 2017, **6**, M3078.

124 L. Kegelmann, C. M. Wolff, C. Awino, F. Lang, E. L. Unger, L. Korte, T. Dittrich, D. Neher, B. Rech and S. Albrecht, It Takes Two to Tango-Double-Layer Selective Contacts in Perovskite Solar Cells for Improved Device Performance and Reduced Hysteresis, *ACS Appl. Mater. Interfaces*, 2017, **9**, 17245–17255.

125 C. Tian, E. Castro, T. Wang, G. Betancourt-Solis, G. Rodriguez and L. Echegoyen, Improved performance and stability of inverted planar perovskite solar cells using fulleropyrrolidine layers, *ACS Appl. Mater. Interfaces*, 2016, **8**, 31426–31432.

126 C. Tian, S. Zhang, A. Mei, Y. Rong, Y. Hu, K. Du, M. Duan, Y. Sheng, P. Jiang, G. Xu and H. Han, A Multifunctional Bis-Adduct Fullerene for Efficient Printable Mesoscopic Perovskite Solar Cells, *ACS Appl. Mater. Interfaces*, 2018, **10**, 10835–10841.

127 C. Tian, K. Lin, J. Lu, W. Feng, P. Song, L. Xie and Z. Wei, Interfacial Bridge Using a *cis*-Fulleropyrrolidine for Efficient Planar Perovskite Solar Cells with Enhanced Stability, *Small Methods*, 2019, 1900476.

128 J. Chang, Y.-C. Wang, C. Song, L. Zhu, Q. Guo and J. Fang, Carboxylic ester-terminated fulleropyrrolidine as an efficient electron transport material for inverted perovskite solar cells, *J. Mater. Chem. C*, 2018, **6**, 6982–6987.

129 Z. Luo, F. Wu, T. Zhang, X. Zeng, Y. Xiao, T. Liu, C. Zhong, X. Lu, L. Zhu, S. Yang and C. Yang, Designing Perylene Diimide/Fullerene Hybrid as Effective Electron Transporting Material in Inverted Perovskite Solar Cells with Enhanced Efficiency and Stability, *Angew. Chem., Int. Ed.*, 2019, **58**, 8520–8525.

130 J. Han, H.-Y. Wang, Y. Wang, M. Yu, S. Yuan, P. Sun, Y. Qin, Z.-X. Guo, J.-P. Zhang and X.-C. Ai, Efficient promotion of charge separation and suppression of charge recombination by blending PCBM and its dimer as electron transport layer in inverted perovskite solar cells, *RSC Adv.*, 2016, **6**, 112512–112519.

131 C. Tian, K. Kochiss, E. Castro, G. Betancourt-Solis, H. Han and L. Echegoyen, A dimeric fullerene derivative for efficient inverted planar perovskite solar cells with improved stability, *J. Mater. Chem. A*, 2017, **5**, 7326–7332.

132 S. Yang, T. Wei and F. Jin, When metal clusters meet carbon cages: endohedral clusterfullerenes, *Chem. Soc. Rev.*, 2017, **46**, 5005–5058.

